Earth Obs., 1, 207–232, 2026
https://doi.org/10.5194/eo-1-207-2026
© Author(s) 2026. This work is distributed under
the Creative Commons Attribution 4.0 License.

Earth Observation

Research article

Towards best practices in UAV thermal remote sensing in complex environments

Kathrin Naegeli[1], **Jennifer Susan Adams**[1], **Gabriele Bramati**[1], **Isabelle Gärtner-Roer**[1], **Julian Gröbner**[2], **and Nils Rietze**[1,3]

[1]Department of Geography, University of Zurich, Winterthurerstrasse 190, 8057 Zurich, Switzerland
[2]Physikalisch-Meteorologisches Observatorium Davos, World Radiation Center (PMOD/WRC), Dorfstrasse 33, 7260 Davos Dorf, Switzerland
[3]Department of Evolutionary Biology and Environmental Studies, University of Zurich, Winterthurerstrasse 190, 8057 Zurich, Switzerland

Correspondence: Kathrin Naegeli (kathrin.naegeli@geo.uzh.ch)

Received: 9 February 2026 – Discussion started: 18 February 2026
Revised: 28 October 2026 – Accepted: 2 November 2026 – Published: 19 November 2026

Abstract. Thermal infrared (TIR) remote sensing using uncrewed aerial vehicles (UAVs) is a promising approach for measuring surface temperatures in complex environments. This study examines the challenges encountered and the lessons learned from UAV TIR surveys of a cryospheric landform in the Swiss Alps. We conducted laboratory experiments and field observations to develop, implement and evaluate the effectiveness of different correction schemes. The results reveal significant dependencies between the internal temperature of the camera and the retrieved surface temperatures, showing a non-linear bias of the UAV TIR camera towards cold, warm, and hot targets. The correction schemes produce divergent outcomes; some amplify extremes, while others reduce the temperature spatial distribution. Validation against data from in situ TIR radiometers and ground surface temperature loggers shows that field calibration provides the most accurate results, whereas drift correction can be misleading in environments with complex topography. By addressing technical and environmental limitations, we provide best practices for UAV TIR surveys and post-processing strategies. Our findings highlight the importance of robust calibration, topographic characterisation and site-specific validation to accurately retrieve surface energy budget-relevant variables in rapidly changing mountainous environments.

1 Introduction

Mountain regions are warming faster than the global average (Pepin et al., 2025, 2022), with wide-ranging impacts on their ecosystems, and especially the cryosphere (Tricht et al., 2025). These changes alter the composition of Earth's surface, for example through transitions from ice to rock or grass to shrub. Such transitions significantly affect the energy exchange between the surface and the atmosphere and the Surface Energy Budget (SEB). Earth system models quantify SEB dynamics across space and time and are therefore crucial for projecting changes under continued warming. However, they require accuarte representations of SEB-relevant variables, which are difficult to obtain in these complex environments, creating uncertainty in projections. Land Surface Temperature (LST), a recognised Essential Climate Variable by the Global Climate Observing System, is fundamental to surface-atmosphere energy exchange and central to SEB. It is closely linked to the radiative, latent, and sensible heat fluxes and varies strongly across space and time (Crago and Qualls, 2014). LST can be spatially quantified using remotely sensed thermal infrared imagery from various platforms, including Uncrewed Aerial Vehicles (UAVs), airborne sensors such as HyTES (Hook et al., 2013) and TASI (Pignatti et al., 2011), and upcoming satellite missions such as TRISHNA (Thermal infraRed Imaging Satellite for High-resolution Natural resource Assessment; Roujean et al., 2021), SBG (Surface Biology and Geology; Cawse-Nicholson et al., 2021) and

LSTM (Land Surface Temperature Monitoring; Koetz et al., 2018).

Traditionally, LST research on cryospheric landforms has relied on either in situ measurements or satellite observations, both of which have limited spatial or temporal coverage (Aubry-Wake et al., 2022). In complex environments, LST retrieval is particularly affected by small-scale heterogeneity that cannot be captured by point-scale in situ instruments or coarse-resolution satellite data. Studies have also shown that scaling LST data across space and time is challenging and that assimilating products at intermediate spatial and/or temporal scales is advantageous (Elfarkh et al., 2023), especially in rugged mountain terrain. UAVs have emerged as an important intermediate platform, bridging the gap between in situ data and satellite remote sensing by providing sub-meter resolution data (Colomina and Molina, 2014; Bhardwaj et al., 2016). The use of UAVs, also carrying thermal sensors substantially increased in recent years (Messmer and Groos, 2024; Bisset et al., 2023; Gök et al., 2023; Kraaijenbrink et al., 2018). However, because high-resolution (sub-meter-scale) datasets remain scarce, synergies between close-range and satellite remote sensing remain underexplored (Kraaijenbrink et al., 2018). Mismatches between concurrent observations from these platforms are attributed mainly to unknown biases from scaling effects (Groos et al., 2022) and/or differences in survey timing (Bisset et al., 2023)which can produce temperature divergences of several degrees (Kraaijenbrink et al., 2018; Liu et al., 2006). Despite the increased use of UAV TIR remote sensing to map LST, accurate surface-temperature retrieval remains challenging, particularly in complex environments. Here, complex environments are defined as settings with steep topography, strong elevational gradients, and highly heterogeneous (sub-)surface conditions that produce large contrasts in microclimate and surface properties. Fully exploiting technological advances therefore requires addressing the methodological challenges that complicate LST retrieval in rugged alpine terrain.

UAV TIR measurements face several technical hurdles. Uncooled microbolometer sensors, widey used onboard UAV platforms, are particularly susceptible to camera temperature drift as they warm or cool during the flight. This drift produces a camera–target temperature dependency, whereby retrieved target temperatures vary with camera temperature; wind and solar irradiance are the strongest environmental controls on this relationship (Gök et al., 2023; Wang et al., 2023; Wigmore and Molotch, 2023; Casas-Mulet et al., 2020; Dugdale et al., 2019; Lin et al., 2018). Stabilising the camera temperature is therefore essential for accurate data acquisition but has often required custom modifications (Arioli et al., 2024; O'Sullivan and Kurylyk, 2022). Strategies such as pre-flight warm-up (Kelly et al., 2019) or additional flight lines in the beginning of a survey (Bisset et al., 2023), provide only partial solutions, because ambient conditions may continue to change during the flight. As such variability is particularly pronounced in complex environments, controlled laboratory characterisation can identify general camera–target temperature dependencies and support drift correction. Improved mosaicking schemes that account for variable ambient conditions may also help (Malbéteau et al., 2021), although their implementation in complex environments remains difficult. Target properties compound these acquisition challenges. Surface emissivity is often assumed to be uniform, but varies substantially across natural landforms and surface types, from debris to ice cliffs to snow. If uncorrected, this emissivity variability can systematically bias retrieved LST (Bisset et al., 2023; Colombo et al., 2023). Reference panels and exposed ice cliffs at 0 °C have been proposed for calibration (Gök et al., 2023; Kraaijenbrink et al., 2018), but biases may still fluctuate under dynamic atmospheric conditions (Maes et al., 2017). These intertwined acquisition and target-related challenges demonstrate the need for systematic laboratory testing and well-designed field campaigns to develop robust correction and calibration frameworks, that allow exploiting the full potential of UAV TIR observations of entire landforms situated in complex environments.

Beyond these technical challenges, environmental heterogeneity strongly influence the accuracy of LST retrieval in complex terrain. Rough surfaces such as rock glaciers or debris-covered glaciers, to name two cryospheric landforms, are affected by shading from steep topography, large elevational gradients, and microclimatic variability, which can produce temperature contrasts of several degrees within a single landform (Huo et al., 2021; Brenning et al., 2012). Contrasting surface materials such as ice cliffs and debris or rocky patches and vegetation have different thermal responses that further increase within-flight variability. Atmospheric effects, particularly wind and sudden cloud cover, compound this variability by altering both camera temperature and target emission during data acquisition. Satellite sensors with long revisit times often miss this fine-scale variability (Lillesand et al., 2015), whereas UAVs provide the spatial detail and revisit capability needed to map parts or entire landforms at sub-meter resolution and disentangle environmental controls on LST (Kraaijenbrink et al., 2016). Nevertheless, the effects of contrasting surfaces on LST retrieved from UAV and coarser-resolution satellite data remain insufficiently assessed. Without appropriate correction and calibration, environmental heterogeneity can also propagate into systematic errors in derived parameters, including debris thickness on debris-covered glaciers and snow thermal state (Bisset et al., 2023; Colombo et al., 2023).

This study aims to improve the accuracy of UAV TIR observations in complex environments. Specifically, we (i) quantify how correction approaches affect TIR orthomosaics (TIR OMs) and (ii) discuss how topographic factors influence retrieved LST and its validation against in situ measurements. These objectives are addressed through analyses and experiments conducted before, during, and after data ac-

quisition, including a sensitivity analysis of the applied corrections. Based on the results, we provide practical recommendations for UAV TIR surveys in complex environments, working towards a standard acquisition protocol. This work supports more accurate retrieval of SEB-relevant variables and the use of UAV observations alongside upcoming satellite missions providing TIR data at unprecedented spatial and temporal resolutions.

2 Study site and data

We conducted UAV TIR surveys in the upper Engadine valley in southeastern Switzerland. The mean air temperature recorded at the station located on Murtèl rock glacier within the UAV survey area is −1.66 °C (for the period 1997–2018; Hoelzle et al., 2022) and the mean annual precipitation sum at the MeteoSwiss station located at the valley bottom in Sils Maria is 1011 mm, whereas the station on Piz Corvatsch recorded a sum of 1295 mm (for the period 1981–2010). The area is at the lower permafrost limit and comprises rock glaciers with different activity status, from low-elevation relict rock glaciers in permafrost-free areas to high-elevation, ice-rich active rock glaciers and perennially frozen talus slopes. The survey area is part of the latter and the active rock glacier area comprising both Murtèl and Marmugnun is depicted manually based on RGB and terrain information (Fig. 1a). These rock glaciers have been monitored and instrumented for over 30 years (Gärtner-Roer and Hoelzle, 2021) and they consist of coarse blocky surfaces with a thickness of about 3–6 m above a 25 m thick ice supersaturated permafrost layer (Saibene et al., 2026). The surveyed area spans an elevation range from 2440 to 2760 m a.s.l. (Fig. 1c) and an average slope of 25 ± 14° (Fig. 1e). The rocks consist predominantly of Metagranitoids of all sizes and the vegetation in the lower parts of the survey area is characterised by alpine meadows. We used the UAV RGB imagery to classify the survey area into rock and vegetation (Fig. 1d). This is resulting in an object-based emissivity characterisation of the survey area of 0.92 for the pixels classified as rocks (Mineo and Pappalardo, 2021) and 0.96 for the vegetation pixels (Rubio et al., 1997), respectively.

2.1 UAV-based TIR surveys

The UAV surveys took place on 23 August 2022 and 22 August 2023 in clear-sky conditions around local noon (CEST+2). A fixed-wing eBee X with a Duet T camera (sensefly, https://ageagle.com/drones/ebee-x/, last access: February 2026) was used. The Duet T camera is a dual mapping system comprising a high-resolution, radiometric thermal infrared camera (FLIR Tau 2) operating in the 8–14 µm range and a S.O.D.A. RGB camera. The flight altitude was with 220 m above ground rather high but needed due to cables obstructing a lower flight level. Each UAV survey lasted for about 20 min (23 min in 2022 and 22 min in 2023) and covered a total area of 0.53 km^2. The surveys were planned in way that camera temperature could possibly stabilise before the image acquisition starts. Hence, the UAV take off was at lower elevation in front of the survey area and the flight pattern started in the south-eastern, most elevated corner of the survey area. We flew the UAV in the terrain following flight mode, perpendicular to the solar principal plane to avoid hot spot/glint and large shadowing effects, as well as minimising directionality impacts. To geolocate our images we used Post Processing Kinematic (PPK) with data from the Swiss Positioning Service (swipos). We collected 510 and 501 RGB and thermal images in 2022 and 2023, respectively. Metadata including the internal temperature of the camera was extracted from the exif file accompanied by each TIR image. This configuration and the use of the Duet T processing work flow and template for the sensefly DuetT camera for pix4d mapper (SenseFly Pix4D Duet T camera processing template: https://support.pix4d.com/hc/en-us/articles/360000173463, last access: February 2026) resulted in RGB and thermal orthomosaics with ∼ 16 cm Ground Sampling Distance (GSD). As a last step, the differently corrected TIR orthomosaics were resampled to 20 cm GSD to ensure optimal comparison between years and datasets.

2.2 Meteorological data

There is a long-term full energy balance station operated by the Swiss Permafrost Monitoring Network (https://www.permos.ch, last access: February 2026) located in the centre of Murtèl rock glacier (Fig. 1a) providing temporally highly resolved (every 10 min) meteorological data. Mean air temperature in the hour spanning the UAV survey was 7.40 ± 0.10 °C in 2022 and 15.52 ± 0.39 °C in 2023, while the surface temperature at the energy balance station showed greater variability with a mean of 8.29 ± 0.58 °C in 2022 and 20.42 ± 1.80 °C in 2023. Wind speed was low in both years with 2.55 ± 0.56 and 1.34 ± 0.23 m s^{-1} for 2022 and 2023, respectively. Relative humidity was 65 ± 7 % and thus considerably higher in 2023 than in 2022 (45 ± 2 %). Net shortwave radiation (defined as $SW_{net} = SW_{in} - SW_{out}$) was slightly higher and less stable in 2023 (663 ± 159 W m^{-2}) than in 2022 (602 ± 23 W m^{-2}). Net longwave radiation (defined as $LW_{net} = LW_{in} - LW_{out}$) was very similar in both years with −120 ± 2 and −118 ± 3 W m^{-2} for 2022 and 2023, respectively. Details about the meteorological conditions 2 d prior and past the survey day, as well as ±30 min from the start of the UAV survey can be found in the Appendix Figs. A1 and A2.

2.3 Auxiliary data

During the survey in 2022, four thermal infrared (TIR) radiometers (Apogee SI-121-SS) were installed (Fig. 1b): while two were placed in vegetated locations in front of Murtèl, one was placed on a ridge and one in a furrow in

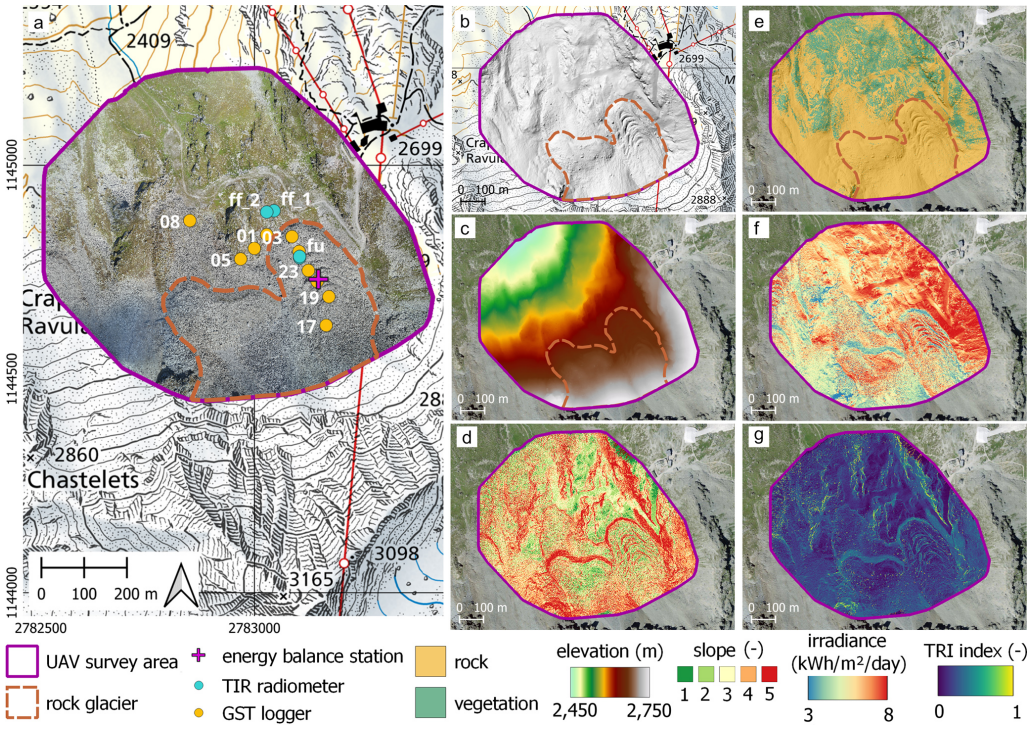

Figure 1. Study site of rock glaciers Murtèl and Marmugnun in the Engadin valley above Silvaplana. **(a)** Topographic map (source: Federal Office of Topography swisstopo) with RGB UAV orthomosaic overlaid incl. location of in situ instruments, UAV survey area and rock glacier extent; **(b)** hillshade of UAV survey area; **(c)** digital surface model; **(d)** slope of UAV survey area in five classes (1: (nearly) flat, 2: gentle, 3: moderate, 4: steep, 5: very steep slope), **(e)** surface classification, **(f)** daily sum of solar radiation for DOY 234, and **(g)** Terrain Ruggedness Index (TRI) after Riley et al. (1999). Panels **(b)** to **(g)** are based on UAV data. Panels **(b)** and **(e)–(g)** display the topographic map and Swissimage true-color imagery as the background, respectively (source: Federal Office of Topography, swisstopo).

the lower third of the rock glacier. The TIR radiometers are operating in the 8–14 µm range with a 18° half angle FOV. Their stated accuracy is 0.2 °C from −30 to 65 °C, when the Δ-temperature between target and sensor is < 20 °C, and 0.6 °C when Δ-temperature is > 20 °C. All TIR radiometers provided us with temporally highly resolved (10 min) radiometric skin temperature information encompassing different footprint sizes (1.6–18.8 m^2) depending on installation height and angle.

Additionally, we had access to Ground Surface Temperature (GST) data at 10 different locations (nine UTL loggers v2 and v3, and one GEO PRECISION M-Log5W, Fig. 1a), four in the forefield and on the relict part of the rock glacier, and six on the rock glacier itself, that provide contact skin temperature data of the top part of the active layer at 60–90 min intervals. The stated accuracy of both logger models is 0.1 °C.

During the survey in 2023, only one TIR radiometer was still installed on the ridge of Murtèl. Simliarly, GST loggers were available but some couldn't be accessed since due to large rock fall activities. Thus, for four GST loggers we do only have data from just the days before the UAV survey, but in similar meteorological conditions (Appendix Fig. A2), and one GST logger was buried ("GST-017").

For field calibration purposes, we built 0.6 × 0.6 m Thermal Calibration Plates (TCPs) following suggestions by Kelly et al. (2019). These side lengths are about 3.75 times larger than the GSD of the TIR mosaics. We used a 1 mm thick aluminium sheet underlaid by a 20 mm thick expanded polystyrene plate for isolation and a 4 mm thick wooden plate for stabilisation purpose. A surface contact PT100 thin-film Resistance Temperature Detector (RTD) (OMEGA SA1-RTD-4W) was attached to the underside of the aluminium sheet, which was painted with black paint with known emissivity ($\varepsilon = 0.963$, HERP-LT-MWIR-BK-11 from LabIR). Temperature readings were recorded using a blueDAN Pt100_4.0 logger every 30 s. In 2023, two TCPs were placed on the rock glacier and one TCP was placed close to the take off and landing point of the UAV. The latter was used to develop and implement the field thermal calibration. The two in-survey TCPs were not used in any subsequent analysis but our learnings included into the discussion.

2.4 Topographic characteristics at validation locations

To assess possible impacts of topographic characteristics on the absolute deviation between in situ observations and TIR mosaics, five topographic metrics, elevation, slope, aspect,

small scale terrain roughness and the irradiance received by the instrument location prior to the UAV survey were assessed. Figure A7 presents these characteristics per individual TIR radiometer and GST location.

The in situ sensors were spread out over an elevational gradient (> 120 m) spanning from 2572 to 2693 m a.s.l. Similarly, the average slope characteristics varied from being flat (1.4° at "GST-04") to very steep (40.4° at "GST-03"), with an average of $19.2 \pm 11°$. Moreover, the variability of slopes (standard deviation) extracted within the footprint of each location varied greatly from ± 1.2 to $\pm 19.3°$ (mean $8.3 \pm 6.2°$), highlighting the very heterogeneous surface characteristics of some in situ instrument locations. This terrain heterogeneity was also well depicted in the Terrain Ruggeddness Index (TRI) (Riley et al., 1999) that showed a range of values from 0.01 to 0.42 (mean 0.17 ± 0.12) depending on the in situ location. The global total irradiance (see Sect. 3) received at each in situ location varied considerably from 4494 $\mathrm{W\,h\,m^{-2}\,d^{-1}}$ at minimum (TIR radiometer "fu") to 7470 $\mathrm{W\,h\,m^{-2}\,d^{-1}}$ at maximum ("GST-04"), with an average of 6494 ± 911 $\mathrm{W\,h\,m^{-2}\,d^{-1}}$ over all in situ locations. Also, the variability of global total irradiance (standard deviation) received within the footprint of each location showed great difference from almost none with 109 $\mathrm{W\,h\,m^{-2}\,d^{-1}}$ (TIR radiometer "ff2") to massive with 1515 $\mathrm{W\,h\,m^{-2}\,d^{-1}}$ ("GST-21").

3 Methdology

Within this study, we define *complex environments* as follows:

- *complex topography* (high altitude sites, large topographical gradients within and surrounding the surveyed landform, remote and hardly accessible) and/or
- *high elevation and/or high elevational gradient* (large gradient in atmospheric conditions within the survey area) and/or
- *large variance of slope and aspects* (high surface ruggedness) and/or
- *little surface contrast* (uniform surface morphologies/-type) and/or
- *high spatial heterogeneity* (small-scale characteristics within survey area) and/or
- *complex sub-surface–surface–atmosphere energy exchange* (varying sub-surface materials, heterogenous turbulent and ground heat fluxes) and/or
- *harsh environmental conditions* (very cold, winds, great Δ-temperature between sensor and target)

The RGB orthomosaic and Digital Surface Model (DSM) were used to compute an object-based surface classification (Fig. 1e), which itself is the basis for the spatially distributed emissivity characterisation based on literature values. The computed slope, aspect and DSM served as inputs to compute the irradiance distribution, the total amount of energy received per square meter over the course of one day (DOY = 234 in 2023) calculated using the R.sun.insoltime tool in QGIS (https://grass.osgeo.org/grass-stable/manuals/r.sun.html, last access: February 2026) for the greater survey area. Each correction scheme is characterised by specific processing steps, which we outline hereafter in detail.

To account for the local atmospheric conditions during the surveys ($T_{\mathrm{corr_ATMO}}$, see Fig. 2), we converted the raw binary FLIR images to temperature utilising the R raw2temp function (Tattersall, 2021). The function applies standard radiometric calibration processing equations of thermal infrared images, taking into account the FLIR camera calibration coefficients and local environmental conditions including air temperature, relative humidity and distance to object. Most UAV processing softwares apply these formulae using standard values of environmental variables, thus we updated the conversion using the aforementioned variables monitored by the meteorological station during the survey and the UAV-surface distance used in the survey flight planning (220 m).

Finally, all TIR orthomosaics are emissivity corrected using the emissivity characterisation and the sky temperature T_{bg} following Maes and Steppe (2012):

$$T_{\mathrm{bg}} = \sqrt[4]{\frac{\mathrm{LW_{in}}}{\sigma}} \tag{1}$$

and

$$T_{\mathrm{corr_EMI}} = \sqrt[4]{\frac{T_{\mathrm{meas}}^4 - (1-\varepsilon)\cdot T_{\mathrm{bg}}^4}{\varepsilon}} \tag{2}$$

to obtain emissivity corrected radiometric skin temperature $T_{\mathrm{corr_EMI}}$. With $\mathrm{LW_{in}}$ denoting the incoming longwave radiation, σ the Stefan-Boltzmann constant, ε the emissivity, and T_{meas} the radiant temperature obtained from the UAV TIR camera.

Besides these general characterisation of atmospheric and emissivity effects, we implement three additional, individual correction methodologies to address (i) the camera–target temperature dependency, (ii) the camera temperature drift, and (iii) the potential of temperature control panels (TCPs) in the field. The target temperature reading is always denoted as T_{raw}, i.e. the pixel temperature value in the acquired image, the camera temperature is always denotes as T_{camera}, i.e. the internal temperature of the uncooled microbolometer camera recorded per acquired image. An overview of our full methodological workflow is shown in Fig. 2.

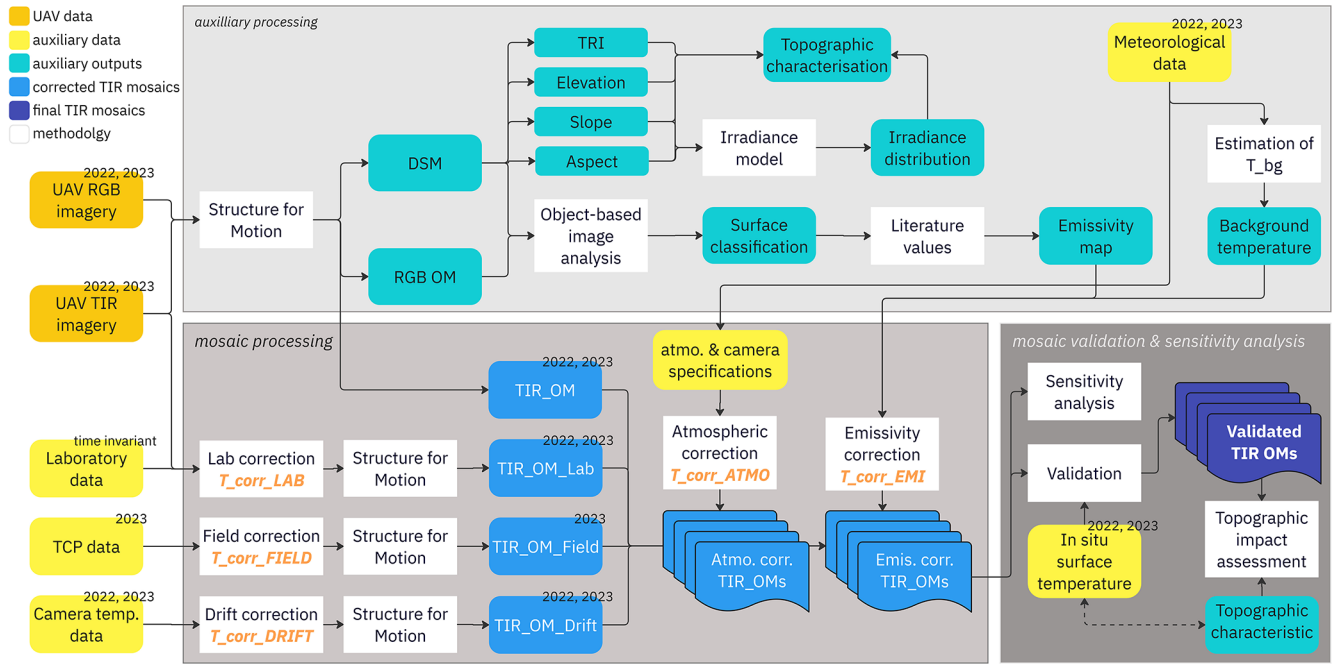

Figure 2. Methodology flowchart showing the auxiliary processing based on the UAV data (top), the processing from individual images to mosaics (bottom left), and the validation and sensitivity analysis of the mosaics, as well as the topographic impact assessment (bottom right). The atmospheric and camera specifications include relative humidity, reflected apparent temperature, radiometeric camera characteristics and distance to object.

3.1 Camera–target temperature dependency correction based on laboratory experiment

In order to investigate the effect of camera–target temperature dependency, we performed laboratory experiments with our DuetT camera at the Physical Meteorological Observatory in Davos (PMOD) World Radiation Centre (WRC) blackbody calibration facilities. The camera was facing into a black body cavity, BB2007, that consists of a custom-made cylindrical cavity with an inclined bottom and an effective emissivity of 0.99993 ± 0.00033 (Gröbner, 2008). Images were acquired every 30 s and the experiments lasted several hours to allow the black body to stabilise at varying temperatures likely to be encountered at the rocky surface of a rock glacier in summer. The radiation temperature at the output aperture of the blackbody is traceable to the SI with a standard uncertainty of 0.05 K. The camera was exposed to simulated wind to (i) not overheat and (ii) have varying camera temperatures alongside stable black body temperatures. Other ambient conditions were kept constant in order to clearly identify the dependence between camera and target temperature. In total these experiments resulted in five stable blackbody set points at approximate mean temperatures of 30, 20, 17, 2.5 and 1 °C alongside camera temperatures in the range of approximately 25–35 °C depending on the individual experiment.

For further analyses, we only used the images that were taken in periods when the black body was stable, i.e. standard deviation smaller than 0.15 °C. This left us with 149 individual images from which we extracted a central area of 320×320 pixels, which we were confident represented the centre of the blackbody and thus limitedly impacted by vignetting effects. From this central area, we randomly sampled 500 pixels (T_{raw}), assigned 80 % of them to train a correction model and 20 % to validate it. Additionally, the camera temperature (T_{camera}) for each of these images and the relating black body temperature were extracted from the metadata. Based on these observations, a second order polynomial multivariate regression model was fit to the data, given inputs T_{raw} and T_{camera}:

$$T_{\mathrm{corr_LAB}} = 0.0 + 1.335 T_{\mathrm{raw}} - 0.327 T_{\mathrm{camera}} + 0.004 T_{\mathrm{raw}}^2 - 0.020 T_{\mathrm{raw}} \cdot T_{\mathrm{camera}} + 0.010 \quad (3)$$

Figure 3a shows the results of the final model on the validation dataset. The model is able to reduce RMSE from 1.98 to 1.086 °C. Higher order polynominal models were tested and resulted in better RMSE, but were omitted as the risk of overfitting temperatures above and below the blackbody temperatures is too high. Figure 3b shows the ratio between target temperature and blackbody temperature with regards to camera temperature, and associated histogram of values (Fig. 3c). The correction model improves reproduction of the blackbody temperature significantly (when ratio equals 1), particularly for lower camera temperatures.

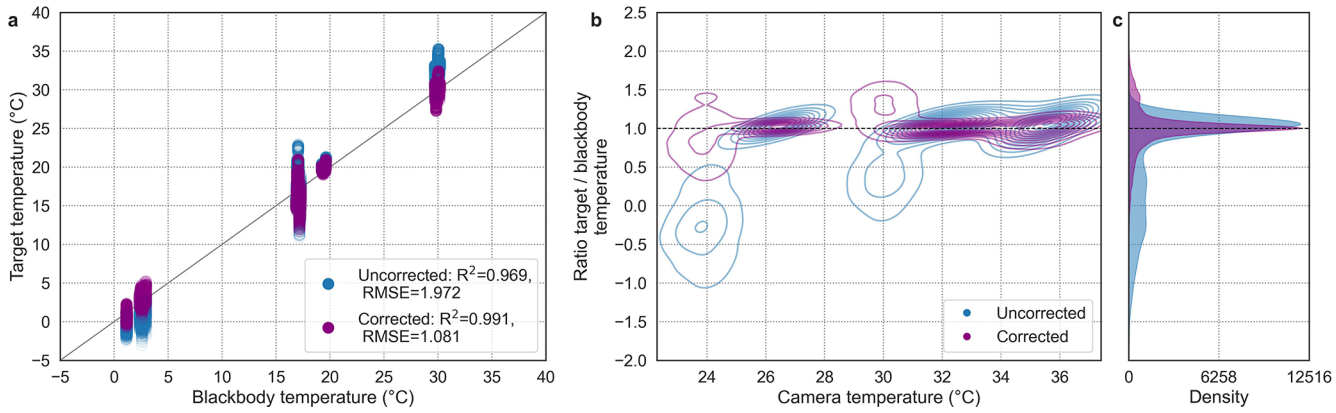

Figure 3. Blackbody reference temperature and associated measured target temperature (T_{raw}) for uncorrected and corrected data using the lab correction model **(a)**, and ratio of target temperature to blackbody temperature with respect to camera temperature (T_{camera}) shown as a Guassian kernel density plot **(b)** and distribution of ratio values **(c)** for uncorrected and corrected data.

3.2 Camera temperature based drift correction

To correct for the impact of changing camera temperature (T_{camera}) on the measured target temperature (T_{raw}), we applied an image-based method adapted from Mesas-Carrascosa et al. (2018) and first used on DuetT thermal imagery in the Arctic tundra in Rietze et al. (2024). The correction relies on in-survey knowledge to derive a relationship between the camera temperature once stable and the related target temperature. It doesn't imply that the target temperature remains constant through the UAV survey, however it was developed for homogeneous surfaces (in texture, topography and surface types) that also exhibit a homogenous surface temperature distribution pattern.

Specifically, this method shifts images by an empirically derived correction temperature (T_{corr}) in the camera's adjustment phase, i.e. during the time it takes for T_{camera} to stabilise (Fig. 4). Consequently, images taken during camera stability (when $T_{camera} < T_{camera,min} \pm 0.1\,°C$) were not corrected. First, a quadratic function to the relationship between T_{corr} and T_{camera} is fitted to retrieve the fitted T_{corr} for any given T_{camera}:

$$T_{corr} = a \cdot T_{camera}^2 + b \cdot T_{camera} + c \quad (4)$$

where T_{corr} is defined as the deviation of the mean temperature of an individual image ($\overline{T}$) over the period of camera instability from $\overline{T}$ during camera stability. Second, T_{corr} is subtracted from each pixel (T_{raw}) in the entire image resulting in drift-corrected T_{corr_DRIFT}:

$$T_{corr_DRIFT} = T_{raw} - T_{corr} \quad (5)$$

3.3 Field thermal calibration using TCPs

In 2023, one TCP was placed close to the take off and landing point of the UAV to obtain hand-held imagery before and after the survey with the UAV TIR camera. The TCP was covered with a white blanket and kept in the shade to obtain warm values (pre-survey). Consequently, the TCP was left exposed to the solar radiation and thus quickly heated up providing us with a hot (pre-survey) and very hot (post-survey) temperature target. A set of hand-held images ($n = 9$) were taken over the TCP in all three temperature conditions. An average image temperature was extracted form all individual 27 images around the image centre (320 × 320 pixels). These average image temperatures were corrected for the emissivity of the black paint (see Auxiliary data) that we used to coat the TCP by a simple emissivity correction not taking into account the reflected radiation from the background. For each target temperature the calculated mean of nine average image temperatures were compared to the measured TCP temperature. The resulting linear model (Fig. 5) was used to correct the 2023 UAV-based TIR images:

$$T_{corr_FIELD} = 0.85 \cdot T_{raw} + 6.35 \quad (6)$$

3.4 Auxiliary data pre-processing

3.4.1 TIR radiometer correction

Correction for surface emissivity is required for accurate temperature measurements also with TIR radiometers. Radiation received by a sensor is thus comprised of the radiation emitted by the surface and the radiation reflected from the background. Temperatures measured from the TIR radiometer were corrected according to Eqs. (1) and (2) introduced above. Emissivity information for the TIR radiometer location was taken from the object-based emissivity classification (see Sect. 2) and background temperature was derived based on data from the AWS (see Sect. 2.3).

Calibration of the SI-121-SS is traceable to NIST (National Institute of Standards and Technology), however sensor temperature of this uncooled TIR radiometer is known to

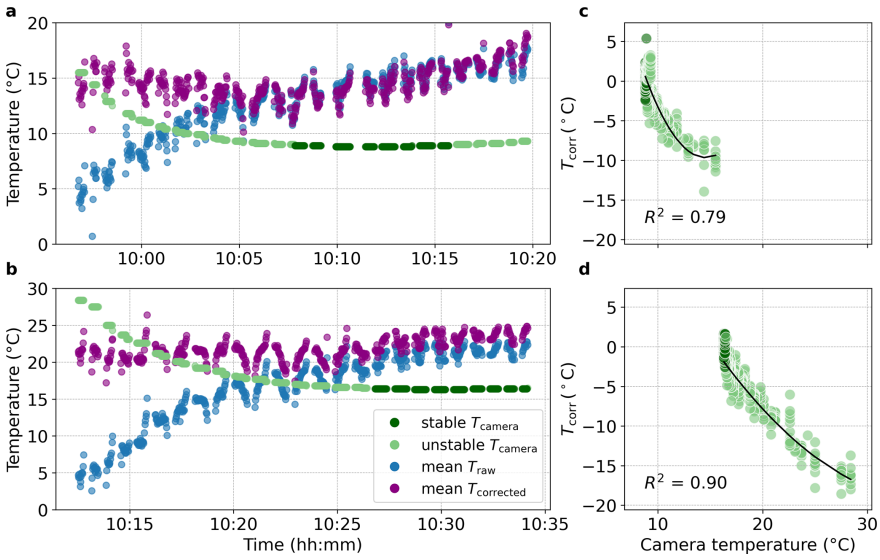

Figure 4. Camera–target temperature dependency during both surveys in 2022 **(a)** and 2023 **(b)** before (blue) and after drift correction (purple). Time shown in panels **(a)** and **(b)** is GPS time. Relationship between camera temperature and correction temperature (T_{corr}) in 2022 **(c)** and 2023 **(d)**.

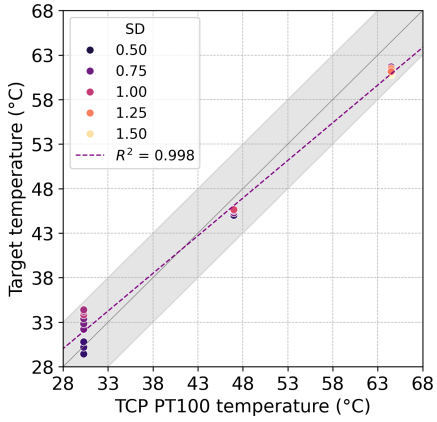

Figure 5. Comparison of pre- and post-flight temperature from the PT100 attached to the TCP and the extracted mean target temperature from the UAV TIR camera imagery ($n = 27$) of the TCP in 2023. Brighter datapoints exhibit larger pixel temperature variability than darker ones.

impact measurement of target temperature and may become biased after their initial calibration (Aragon et al., 2020). Therefore, sensor-target temperature dependency of the TIR radiometers was characterised in the lab following a similar protocol as outlined for the UAV camera and with the same blackbody cavity. A dedicated copper casing for the TIR radiometer was developed to efficiently dissipate heat from the heating plate of the blackbody to alter the sensor temperature. Both the blackbody reference target temperature and the TIR radiometer sensor temperature were set to measure between 0 and 40 °C in steps of 10 °C. Δ-temperature between blackbody and sensor was never more than 20 °C, thus following measurements were made of *blackbody* and sensor (in brackets): *40* (20, 30, 40), *30* (40, 30, 20, 10), *20* (0, 10, 20, 30, 40), *10* (30, 20, 10, 0) and *0* (0, 10, 20). Each blackbody/sensor configuration lasted 40 min (approx. 20 min to stabilise, and 20 min for stable measurements), with both the TIR radiometer and the blackbody measuring at 30 s frequency. TIR radiometer measurements were integrated over 10 s. Finally, a model was developed to correct the measured target and sensor temperature to the blackbody using a 2nd order multivariate polynomial linear regression (Adams et al., 2025).

For the final validation of in situ TIR radiometer data with the differently corrected UAV TIR mosaics, the correction including local emissivity information, the background temperature estimated from incoming longwave radiation measured at the energy balance station and the laboratory correction for the sensor-target dependency was applied.

3.4.2 Pixel extraction

As the TIR radiometers recorded an average temperature of an ellipsoidal footprint, a TIR radiometer specific area (see Sect. 2.3) was extracted from each mosaic for the validation. For the extraction of the pixels around the GST locations, the spot-size-effect (https://www.flir.eu/discover/instruments/electrical-mechanical/how-far-can-you-measure-spot-size-ratio/, last access: February 2026) of the thermal camera and the survey characteristics were taken into account. For our surveys, the spot-size is calculated to be 0.34 m (1 × 1 pixel) and approximately 1 m for 3 × 3 pixels. Consequently, a circular buffer of 1 m diameter was laid around each GST location

to extract the mean and standard deviation for both the temperatures of the different TIR mosaics and the varying topographic characteristics.

3.5 Validation, sensitivity analysis and topographic impact assessment

The outlined correction schemes were implemented at the image level. The final corrected mosaics were validated by calculating the absolute temperature difference between each individual mosaic and the in situ data. To assess the sensitivity of the raw TIR mosaic to individual correction schemes, the temperature distribution and deviations per and in between mosaics were investigated. To shed light on the impact of topographic characteristics, five different metrics (elevation, slope, aspect, TRI and irradiance, Fig. 1c–g) were extracted per in situ sensor location (see Fig. A7), and their mean and standard deviations correlated with the mean absolute temperature difference obtained from the validation (see Fig. A8).

4 Results

4.1 Camera–target temperature dependency

The laboratory experiments revealed that fluctuations in camera temperatures (Fig. 6a and c) and large Δ-temperatures between camera and target (Fig. 6d and e) drive instability and inaccuracy in recorded target temperatures. Figure 6a–e show absolute temperatures for the target, camera and blackbody and for each individual experiments, while Fig. 6f–j show detrended temperature times series by subtracting their respective mean values, thereby removing absolute offsets and emphasising relative temperature fluctuations between the camera, target, and blackbody for clarity of comparison. The correlation between camera and target temperature was positive and stronger for warmer blackbody temperatures, and negative and weaker for blackbody temperatures close to zero. This reflects the camera specifications stating a decreasing accuracy with increasing Δ temperature between target and camera.

The absolute comparison of blackbody versus target temperatures indicated the underestimation of cold and the overestimation of warm blackbody temperatures, respectively (Fig. 7). Experiments that display a greater variability of target temperatures to capture the stable blackbody temperature, are characterised by greater fluctuations in camera temperature (Fig. 6f, h, and k) as well as hotter camera temperatures (Fig. 7), highlighting again the strong dependency between camera and target temperature, as well as the importance to keep the Δ-temperature between camera and target small. Additionally, the results from the experiment with greatest correlation both between camera and target and blackbody (Fig. 6b, g and k), respectively, clearly indicate that a constant camera temperature in combination with a reasonably small Δ-temperature between camera and target results in the most accurate target temperature observations.

4.2 Camera temperature based drift correction

The internal temperature of the camera (T_{camera}) cooled down in the first minutes of both surveys impacting the surface temperature observations (Fig. 4a and b). The R^2 of the fitted models was 0.79 and 0.86 for 2022 and 2023, respectively, indicating a good fit (Fig. 4c and d). The temperature of the raw images (T_{raw}) during the period of highest camera instability, i.e. in the first 10–12 min, had to be corrected by up to approximately 10 and 15 °C in 2022 and 2023, respectively.

4.3 Field thermal calibration

The warm target was overestimated by 2.06 °C, while the hot and very hot targets were underestimated by 1.65 and 3.24 °C, respectively (Fig. 5). The greatest variability was observed for the very hot target temperatures with an average standard deviation of 1.15 °C, and considerably lower average standard deviations of 0.77 and 0.62 for the warm and hot targets, respectively. Overall, this pre- and post-survey thermal field calibration revealed an accuracy of the mean image pixel temperatures of -0.95 ± 0.85 °C, which is far below the stated accuracy for the camera model of ±5 °C, and even including outliers of up to $+4.09 \pm 0.91$ and -3.74 ± 1.60 °C.

4.4 Sensitivity analysis for applied correction schemes

The corrections outlined above have varying impact on the mean pixel temperature of the orthomosaics but also the spatial distribution of pixel temperatures within the entire surveyed area (Figs. 8 and A3). The drift correction has the greatest impact on the observed temperature (Fig. 9 and Table A1). While it warms the mosaic overall by 20 % (+2.72 °C) and 45 % (+7.32 °C) on average for 2022 and 2023, respectively, the range of temperature values was attenuated, i.e. a reduction in temperature gradient across the mosaic was observed (Fig. A4 and Table A1). Particularly, the south-eastern corner of the mosaic, which was flown over first and affected by changes in camera temperature the most, is impacted by this correction scheme most (Figs. 8 and A3).

The correction based on laboratory analysis shows only small deviation from the raw mosaic, with slight warming of 3.5 % on average in 2022 and negligible cooling of −0.1 % on average in 2023, and a slight attenuation of minima and maxima, as well as outlier temperatures. In contrast to the drift correction, which also shows substantial impact, the field thermal calibration using a TCP implemented on the 2023 data cools the mosaic by 27 % (−4.04 °C) on average and amplifies the range of observed values by over 10 °C (Figs. 9 and A3).

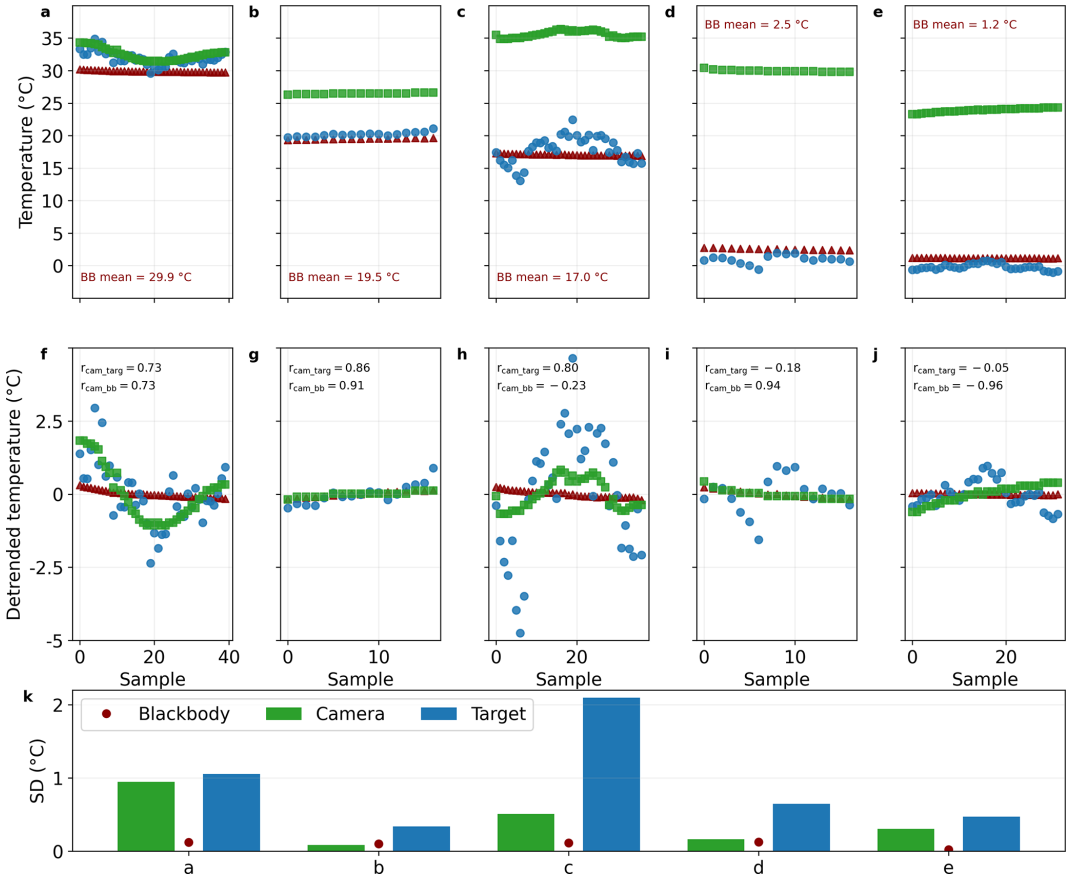

Figure 6. Time series of absolute **(a–e)** and detrended **(f–j)** temperatures of target (blue), camera (green), and blackbody reference temperature (darkred) for five experiments with different blackbody setpoints (BB mean). Correlation coefficients ($r_{\text{cam_targ}}$ and $r_{\text{cam_bb}}$) between camera and target temperatures, and camera and blackbody temperatures, respectively, are given for each experiment in panels **(f)–(j)**. Panel **(k)** summarizes the variability (standard deviation) of target, camera, and blackbody temperatures for all experiments.

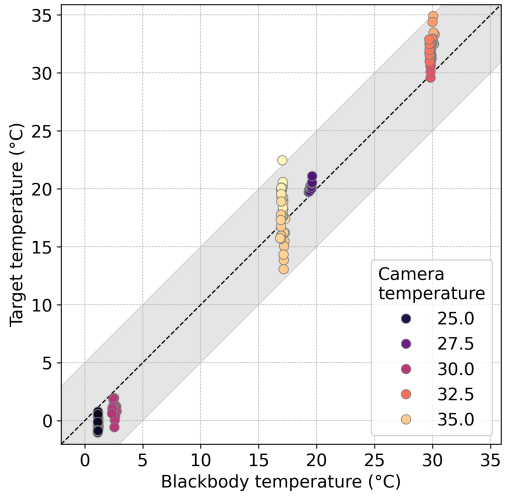

Figure 7. Relationship between blackbody and target temperature for all experiments. Each point represents one image ($n = 27$), colored by its camera temperature. The dashed line indicates the 1 : 1 relation, with the shaded area marking the accuracy range of ±5 °C provided by FLIR for the camera model Tau 2.

4.5 Validation with in situ data

The availability of TIR radiometer and GST data allows for an absolute validation of all TIR OMs keeping in mind that the instruments (UAV TIR camera, TIR radiometers (“ff1”, “ff2”, “ri”, “fu”) and GST loggers (“01” to “23”) are based on different measurement principles (i.e. contact skin versus radiometric skin temperature measurements), affecting the direct comparison. Figure 10a shows the greatest deviation between TIR OM and in situ data for the drift corrected mosaics in both years with absolute errors up to ∼ 20 °C. The laboratory correction scheme corrected mosaic showed similar validation performance as the raw TIR OMs for both years, with generally less deviations compared to the drift corrected ones, but still errors up to about 15 °C. The smallest mean absolute differences are observed for the field corrected TIR OM in 2023, with most absolute deviations around 1 to 5 °C (six out of ten). However, the field correction only improved half of the in situ location, while the drift correction worsened all locations and the lab correction had a generally low impact over all in situ locations (Fig. 10b).

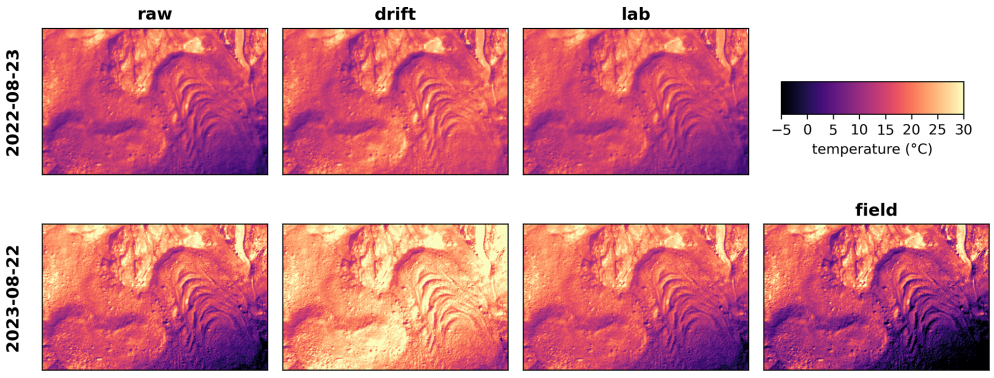

Figure 8. Thermal orthomosaics from both survey years (top: 2022, bottom: 2023, raw data) and varying correction schemes (drift, lab and field).

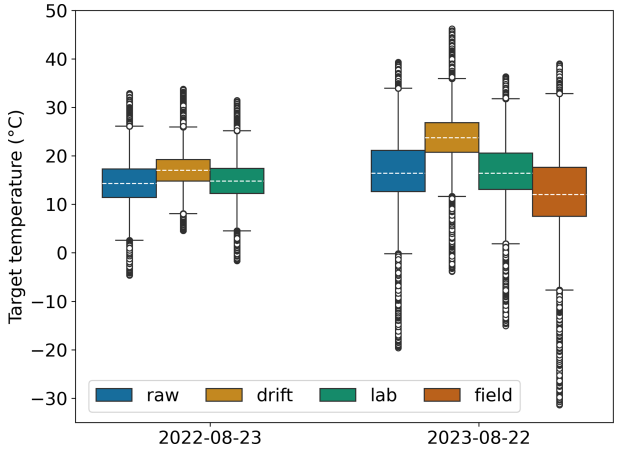

Figure 9. Sensitivity of thermal UAV mosaics to different correction schemes. Boxplots illustrate pixel temperature distributions (°C) for raw mosaic and the drift-, lab-, and field-corrected mosaics on the two survey dates, highlighting the influence of correction choice on the resulting thermal patterns. White dashed line indicates mean value of each orthomosaic.

In light of the stated accuracy range of ±5 °C of the UAV TIR camera, two TIR radiometers show deviations within this range, one is close to this range, and one is off by over 3.5 °C (Fig. 10a, upper part "TIR radiometers"). Generally, the deviations with the GST sensors are greater and only one to four (depending on the correction scheme) are within the accuracy range of the UAV TIR camera (Fig. 10a, lower part "GST").

Focusing on the individual in situ measurement locations, clearly "GST-03", "GST-04", "GST-05" and "GST-08" show greatest deviations, all above 11 °C and up to over 20 °C. In contrast, "GST-01" and the two TIR radiometers "fu" and "ff2" show the most similar temperatures compared to all TIR OMs. The remaining GST locations ("GST-02", "GST-17" to "GST-23") and the two TIR radiometers ("ff1", "ri") show medium deviations in the range of about −4 to 8 °C, except for higher differences if compared to temperature recorded in the drift correct TIR OM.

Local thermal heterogeneity, expressed by the standard deviation of UAV-derived temperatures within each validation extraction area, did not show a consistent association with absolute validation error (Fig. A5). Thermal heterogeneity should therefore be interpreted as a potential source of spatial representativeness uncertainty rather than as a direct predictor of validation error. This is of particular importance when planning the thematic validation in complex environments.

Comparison with the topographic characteristics of the in situ sensor locations (Sect. 2.3 and Fig. A7) suggests that several locations with large absolute validation differences were situated in relatively steep, rough and/or strongly irradiated terrain. However, this pattern was not consistent across all locations or correction approaches. Received irradiance showed the most consistent positive association with absolute validation differences, whereas the relationships with slope and terrain ruggedness were generally weak (Fig. A8a). Locations with absolute differences below (5 °C) were frequently situated in topographically inconspicuous settings or exhibited only one pronounced topographic characteristic, although exceptions occurred. These observations suggest that the combined topographic and radiative setting may contribute to location-specific validation discrepancies but does not independently explain their magnitude.

Overall the TIR OMs corrected with the lab or field correction scheme performed similar to the raw OMs in both years, highlighting the limited correction effect of this approach for our study site (Fig. 10b). The drift corrected TIR OMs show far greater deviations with over 8 and 12 °C in 2022 and 2023, respectively. The best validation performance, with an mean absolute error of ∼6.5 °C on average (∼4 °C if the three strongest outliers ("GST-08", "GST-03" and "GST-04") are omitted), was found for the TIR OM corrected with the field thermal data in 2023.

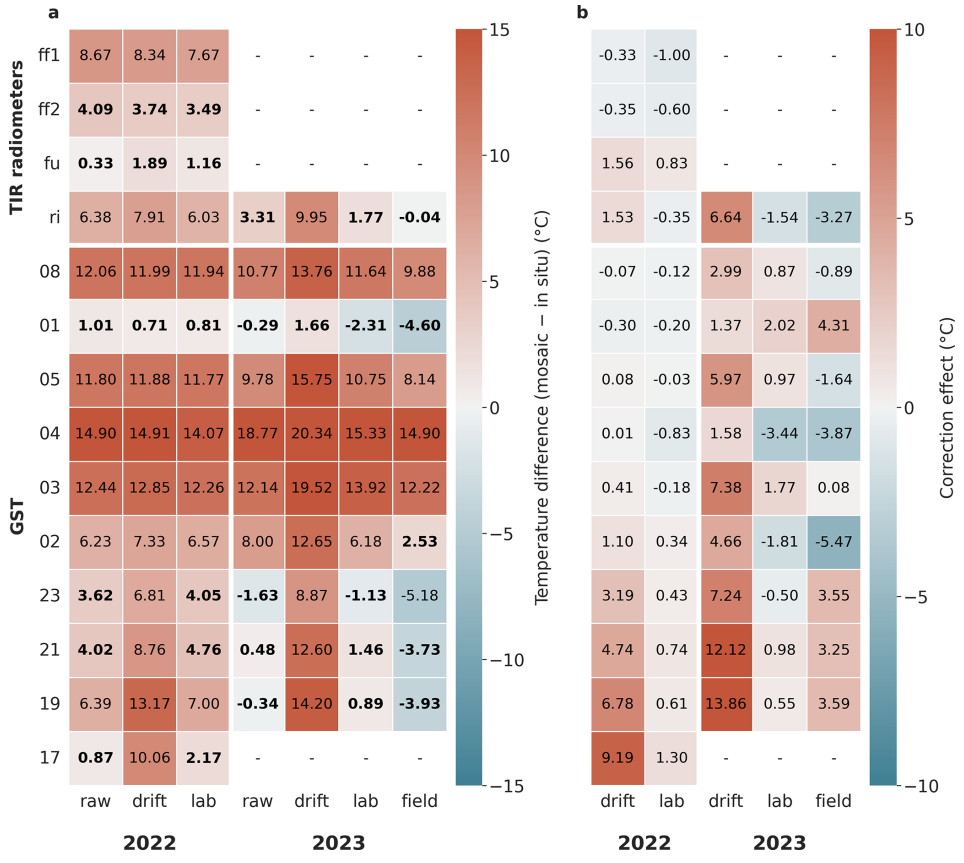

Figure 10. Heatmap of the temperature difference between TIR OMs with in situ data for both years in panel **(a)**. Positive values indicate a warm bias and negative values a cold bias in the orthomosaic. Values with an absolute difference below 5 °C are shown in bold. Correction effect per in situ location in panel **(b)**. Negative values indicate that the correction reduced the absolute error, whereas positive values indicate that it increased the error. Rows are grouped by measurement type into TIR radiometers and GST locations; GST locations are ordered by elevation. Dashes denote unavailable data.

5 Discussion

We conducted various laboratory and field experiments with our UAV TIR camera to characterise its behaviour in response to changing ambient conditions, the dependency between the internal camera temperature and the pixel temperature, and its ability to accurately observe temperatures ranging from cold to very hot. These experiments revealed various challenges and enabled us to develop correction schemes. Based on our lab and field experiments, we demonstrate the UAV TIR camera's non-linear accuracy behaviour towards cold (underestimation), warm (overestimation) and hot (underestimation) target temperatures. Furthermore, the experiments revealed a strong relationship between camera and pixel temperatures, showing that greater variations in the former result in greater variations in the latter. They also demonstrated that this impact increases if the temperature difference between the target and the camera increases, hence Δ-temperature between camera and target should be monitored and ideally the camera temperature stabilised in a way to keep the former minimal. Of the applied correction schemes, the drift correction warms the OM on average, while the field correction scheme cools it, and the lab correction scheme has a negligible impact on the average mean OM temperature. Spatially at the landscape scale of the survey area, the drift correction considerable, and only, warms the south-eastern, most elevated corner, the lab correction slightly warms some areas, while cooling others, and the field correction overall all cools the area with strongest adjustment in the same south-eastern, most elevated corner (Fig. A3). Validation using in situ observations revealed that the field correction scheme performed best, with smallest mean absolute errors, but still only improving validation performance at half of all in situ locations. As the validation has limitations itself, i.e. the comparison of radiometric and contact skin temperature from different sensors, we like to stress the importance of taking physics fully into account when acquiring and processing TIR UAV data rather than solely focusing on performance numbers of the here presented individual correction schemes. Thus, our findings emphasise the importance of careful data acquisition planning, camera characterisation, and highlight the need for and potential of field calibration,

alongside comprehensive post-processing that takes emissivity, atmospheric, environmental and topographic effects into account.

5.1 Prior to data acquisition: camera characterisation, environmental variability and flight planning

Although the lab-based correction scheme had the smallest impact on mean absolute surface temperature it is crucial to gather as much knowledge on temperature dependent camera characteristics in a controlled laboratory setting to ensure minimal surface temperature orthomosaic falsification due to camera internal behaviour. Similarly, experiments should be performed to characterise in situ instruments and their behaviour towards changes in ambient conditions, internal temperature variations and Δ-temperature between sensor and target.

Besides these lab-based preparatory analysis, a thorough analysis of the survey area in terms of topographic characteristics is inevitable in complex environments. Small-scale heterogeneity can be demonstrated by calculating metrics such as the TRI or the spatial distribution of pixel-based received irradiance prior to the planned survey. Classic topographical parameters such as slope, aspect and elevational gradient further help to best characterise the study site and understand surface temperature patterns. Such a detailed investigation of the field site enables the most effective planning of thematic validation, ensuring that the spatial heterogeneity of emissivity, topography, and the resulting surface temperature in the survey area are captured optimally.

Additionally, the flight planning in complex environments is absolutely crucial. The acquisition pattern should be designed based on the characterisation of the UAV TIR camera and the field site. Terrain following flight mode is highly beneficial for sites with large elevational gradients. In order to accurately retrieve surface temperatures, it is necessary to minimise the effects of directionality by taking the flight geometry into account in relation to the position of the sun. Although a survey conducted around local noon is ideal, local topographic characteristics (e.g. shading) may necessitate an earlier or later acquisition time.

5.2 During data acquisition: field thermal calibration and in situ observations

The field-based correction scheme resulted in smallest mean absolute errors highlighting the value of in-field calibration efforts, also shown by other studies (e.g. Wan et al., 2024). The deployed TCPs in the survey area were not useful due to the strong adjacency effects in the data, which resulted from their relatively small size compared to the GSD obtained from the UAV, the spot-size effect of the camera itself as well as the large thermal contrast between the very hot TCPs and the surrounding rocks. However, in the case of our complex study area and flight height a suitable TCP within the survey area would need to have a side lengths of at least 3 m, ideally even more, which is not feasible to bring and deploy in this high altitude, complex terrain.

In contrast, the TCP used to calibrate the camera with handheld pre- and post-survey imagery revealed to be of great help. However, the absolute and range of temperature values covered by this TCP were far from ideal as they did neither mimic the absolute nor the distribution of temperature in the survey areas a suggested by Kelly et al. (2019). This likely explains partially the still multiple degrees of absolute temperature difference at most validation locations.

Furthermore, the positioning of certain GST instruments hampers validation performance as they are heavily shaded by a large boulder, resulting in different temperature readings to those observed by the UAV TIR camera. Similarly, locations that receive great amounts of irradiance prior to the UAV flight heat up more, resulting in higher radiometric temperatures observed by a UAV TIR camera. In contrast, these locations exhibit a lagged temperature cycle in the measured skin temperature culminating with maximum daily temperatures around mid- to late afternoon (Fig. A6) limiting direct validation.

While the existing full energy balance station records data every 10 min, we still noted changing ambient conditions in our field journal at finer temporal resolution. In 2023, the occurrence of few clouds in the vicinity of our survey area, was also visible in the shortwave incoming radiation data. This helped to understand the slight dip in the warming of the GST sensors (see "GST-01" or "GST-03" in Fig. A6). This might also explain parts of the contrasting general temperature behaviour, i.e. underestimation of a few, most elevated GST locations, compared to 2022.

5.3 Post data acquisition: camera temperature drift, thematic validation and topographic impact assessment

We clearly detected cooling of the camera temperature in the beginning of both of our surveys. However, the drift correction applied is clearly not the ideal correction scheme for surveys conducted in complex environments as already stated in the respective methodology section. While this correction was developed for flat tundra sites, our field site was affected by varying degrees of shading due to the surrounding topography, which most likely induced surface temperature gradients across the survey area and affects local thermal inertia. This is also supported by the calculated spatial pattern of the total global irradiance received before the survey. It is nearly impossible to disentangle the effects of these multiple factors on surface temperatures, as well as on the UAV TIR camera and the in situ instruments. However, our validation results clearly showed the worst performance of the drift-corrected OMs, indicating its limited applicability in complex environments. Potentially, TCPs or entire parts of the survey area could be covered by repeated imagery to build a robust un-

derstanding of drift effects, however, this is hardly feasible in many complex environments due to harsh conditions and limited UAV capabilities. Nevertheless, we strongly recommend extracting the internal camera temperature throughout the survey and considering correction schemes to account for variability or omitting parts of the surveyed area.

Generally, validation is hampered by the increasing complexity of the area studied. For example, areas with greater slopes are likely affected by directional effects impacting the accurate retrieval of LST from UAV data, or large small-scale heterogeneity of surface characteristics within the UAV footprint (i.e. GSD- and spot-size effect-dependent) limit validation accuracy, just to mention two examples. We calculated Pearson correlation coefficients between in situ and UAV TIR absolute temperature differences and means and standard deviations of topographic factors (Fig. A8). While analysing mean values provides insight into local topographic characteristics and their potential impact on validation performance, analysing standard deviations reveals the potential impact of local heterogeneity on validation performance. The impact of these factors is expected to be particularly severe in complex environments. A moderate positive correlation was found for mean irradiance, indicating its strong importance for accurately retrieving surface temperature information (Fig. A8a). Interestingly, we found mostly negative correlations between standard deviations and absolute UAV - in situ temperature differences, indicating that increasing heterogeneity leads to decreasing mismatch between UAV and in situ (Fig. A8b). This suggests that in more heterogeneous terrain, UAV TIR OMs tends to average over the spatial heterogeneity, making the UAV observation more representative. However, it should be noted that none of the correlations were significant, which may be due to the limited number of validation locations. A more detailed analysis with a greater sample size, or a comparative study of a complex and non-complex environment, would be of great interest and likely reveal more robust results.

At the landscape level within the survey area we can state that lower surface temperatures were recorded at (i) higher elevations, (ii) on north-facing slopes and (iii) on steeper slopes, while higher surface temperatures occurred in areas where an increased amount of irradiance was received (Fig. A9). Overall this mimics a generally expected surface temperature–topography relationship pattern, which is not correction specific, except for the drift correction, which alters this relationship (Fig. A9, column "elevation"). This reorganised spatial temperature pattern is visible in increased correlation between TIR OM drift and irradiance in both years compared to the raw TIR OM (Fig. A9, column "irradiance"). Focusing on the correction adjustments (Fig. A10) the drift correction is dominated by a strong elevation-dependent adjustment, field correction is most closely associated with irradiance, and lab correction introduces weaker and less consistent topographic dependencies.

5.4 Uncertainties and limitations

The object-based emissivity representation ignores mixed-pixel effects, and single literature-based values neglect local characteristics. While the mixed-pixel effect in the case of a UAV survey and a respective GSD of 20 cm in our survey area is minimal, the literature-based emissivity values are rough assumptions and hence may impact surface temperature retrieval considerably. We tested this impact by increasing and decreasing the fixed emissivity values by 0.01, resulting in an average (over all corrections) decrease and increase in mean OM temperature of 0.2 °C, respectively.

The assumption of spatio-temporally constant local environmental conditions during the survey impacts the radiometric calibration and atmospheric correction. However, considering the survey duration of roughly 20 min and the stable weather situation, this effect is likely negligible. Meteorological data with higher temporal resolution from multiple locations within the survey area would be needed to investigate and quantify this uncertainty.

Adjacency effects are critical when spatial heterogeneity is large (Aubrecht et al., 2016), as indicated by the TRI pattern (Fig. 1g) in our study area and demonstrated by our within-survey TCPs, which were too small. This impact is also dependent on the spot-size effect of the camera and thus hard to quantify. Additionally, the surrounding terrain of the landform cause complex scattering mechanics that likely impact local adjacency effects in the study site. Furthermore, the internal settings of the pix4d software while mosaicking the individual images can lead to a distortion of the observed surface temperatures. Again, a quantification thereof was not performed in this study.

The validation was limited by the difference in physically measured temperature resulting from varying instrument measurement techniques. While the UAV TIR camera and TIR radiometers measure radiometric skin temperature, the GST loggers observe contact skin temperature. The extraction of the UAV data in the footprint area of the TIR radiometers and at the locations of the GST loggers is affected by mixed-pixel effects, primarily due to the large spatial heterogeneity of surface characteristics including microtopography and resulting directionality effects. However, other factors also play a role, including the GSD, the spot-size effect of the camera, the geolocation accuracy of the in situ data and the UAV mosaics, as well as the effects of adjacency and the mosaicking processing step in Pix4D. Furthermore, given that LST is highly variable over time, the GST loggers' rather coarse logging interval is not ideal. Nevertheless, the in situ dataset is a valuable means of validating the performance of the various correction schemes applied in this study.

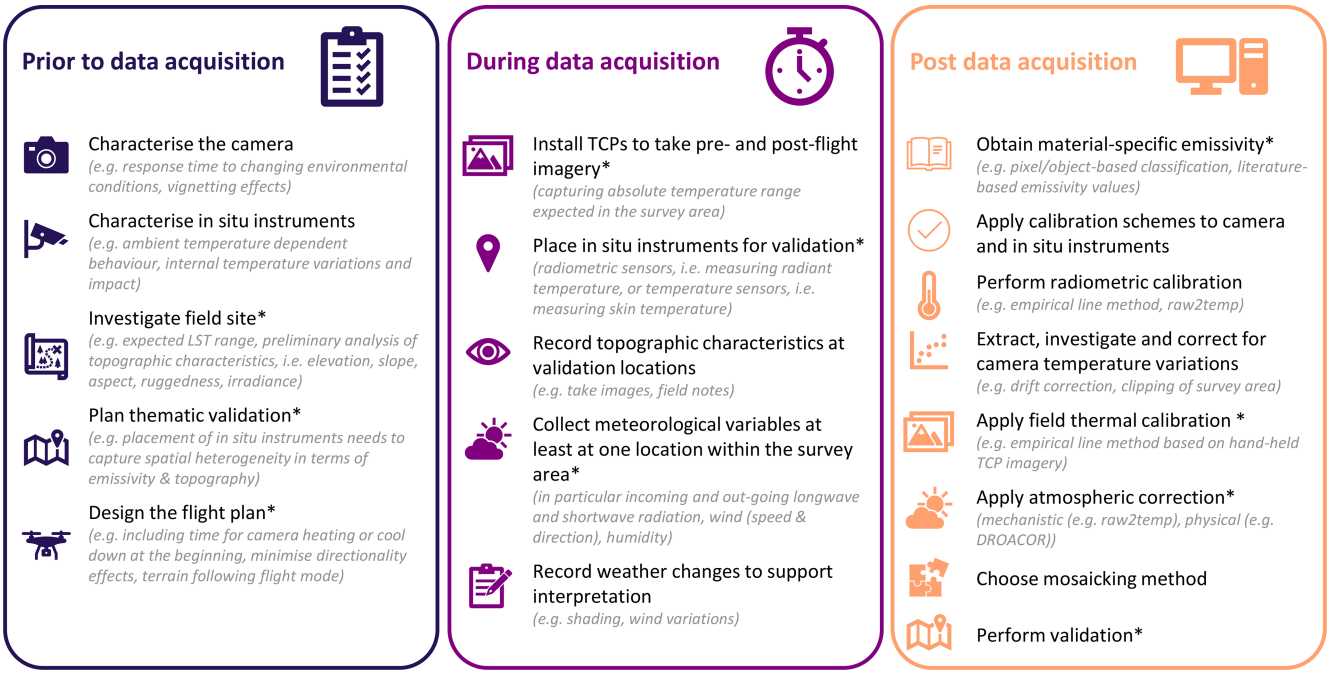

Figure 11. Recommendations for TIR UAV surveys in complex environments. Asterisks (*) mark most important tasks to specifically consider in complex environments.

5.5 Key learnings and recommendations

From our flight planning, laboratory experiments, field data acquisition, post-processing, sensitivity analysis and validation we can state a few key learnings and recommendations for UAV TIR surveys in complex environments (Fig. 11). We provide a set of recommendations forming a basis for more considerations for future studies in this research field. They provide a guideline for points to remember and consider for each individual TIR UAV survey. Additionally, we like to state that many of these points are of relevance for any TIR UAV survey regardless of the site specific characteristics, while some are of particular importance when acquiring TIR UAV data in complex environments (marked with * in Fig. 11).

6 Conclusions

Mountain regions constitute complex environments and are known to change rapidly. Integrative monitoring strategies are required to capture processes related to surface temperature and ultimately the surface energy budget. These strategies should encompass a range of instruments and measurements. UAV TIR surveys offer great potential for monitoring surface temperature in complex environments. However, known challenges such as camera–target temperature dependency and adjacency effects have primarily been investigated in modelling studies, laboratory settings or rather homogeneous, flat environments. This study focused on complex environments that may be particularly susceptible to such disruptive factors.

Thoroughly investigating the heterogeneity within the survey area in terms of per-pixel received irradiance, microtopography and surface materials is key to disentangle the impacting factors as best as possible. Our analysis has demonstrated the importance of field thermal calibration. Pre- and post-flight handheld imaging over TCPs that cover the expected surface temperature range in the survey area is crucial for building a robust calibration model taking field conditions (ambient meteorology and camera behaviour) into account. Proper characterisation of all instruments (in situ and UAV) is essential for interpreting the obtained data and applying the necessary post-processing schemes. While none of the implemented corrections resulted in considerably better validation performance at the landscape scale of the surveyed area, we emphasise the necessity to take TIR physics comprehensively into account when working with such data. Thematic validation adopted to the site specific characteristics greatly supports post-processing, ensuring accurate surface temperature retrieval. Comprehensive knowledge about pre- and post-processing of TIR instruments and data to obtain accurate surface temperature information is key to minimise error propagation down the processing chain such as debris-thickness, albedo and energy fluxes estimations, and related impact on melt/thaw dynamics, to name a few cryospheric examples.

The results of this study shed light on the complexity of acquiring and processing UAV TIR data, specifically high-

lighting the challenges arising from complex environments. We hope similar systematic evaluations of TIR data are performed in other regions and environmental settings to work towards a common survey strategy and physically-based processing protocol for TIR cameras on board UAVs.

Appendix A

A1 Meteorological conditions

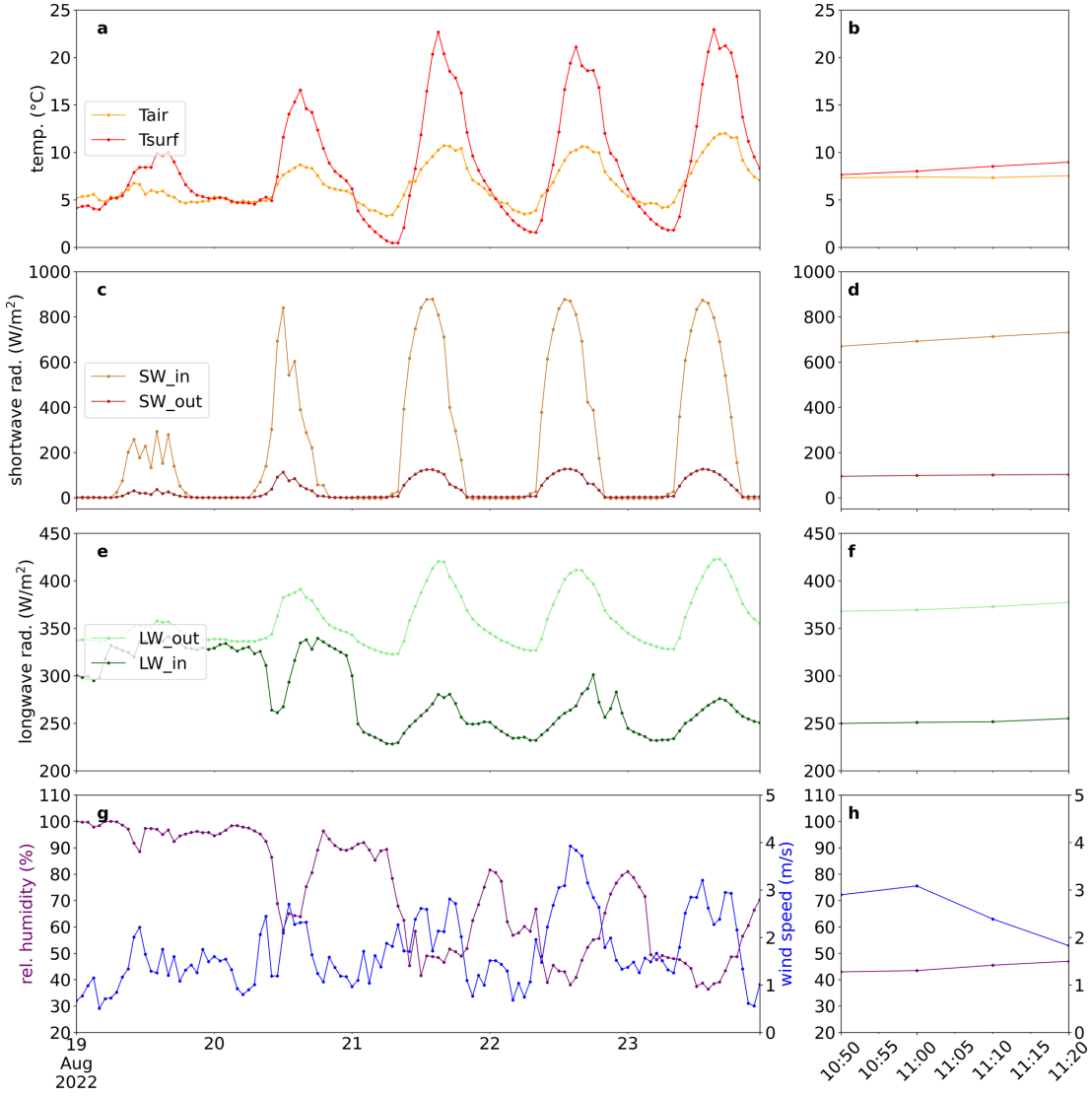

Figure A1. Meteorological conditions at the AWS on the Murtèl rock glacier on the survey day plus 4 d prior (left) and during the survey (right, time shown is GPS time) in 2022 for air and surface temperature **(a, b)**, incoming and outgoing shortwave radiation **(c, d)**, incoming and outgoing longwave radiation **(e, f)**, and relative humidity and wind speed **(g, h)**.

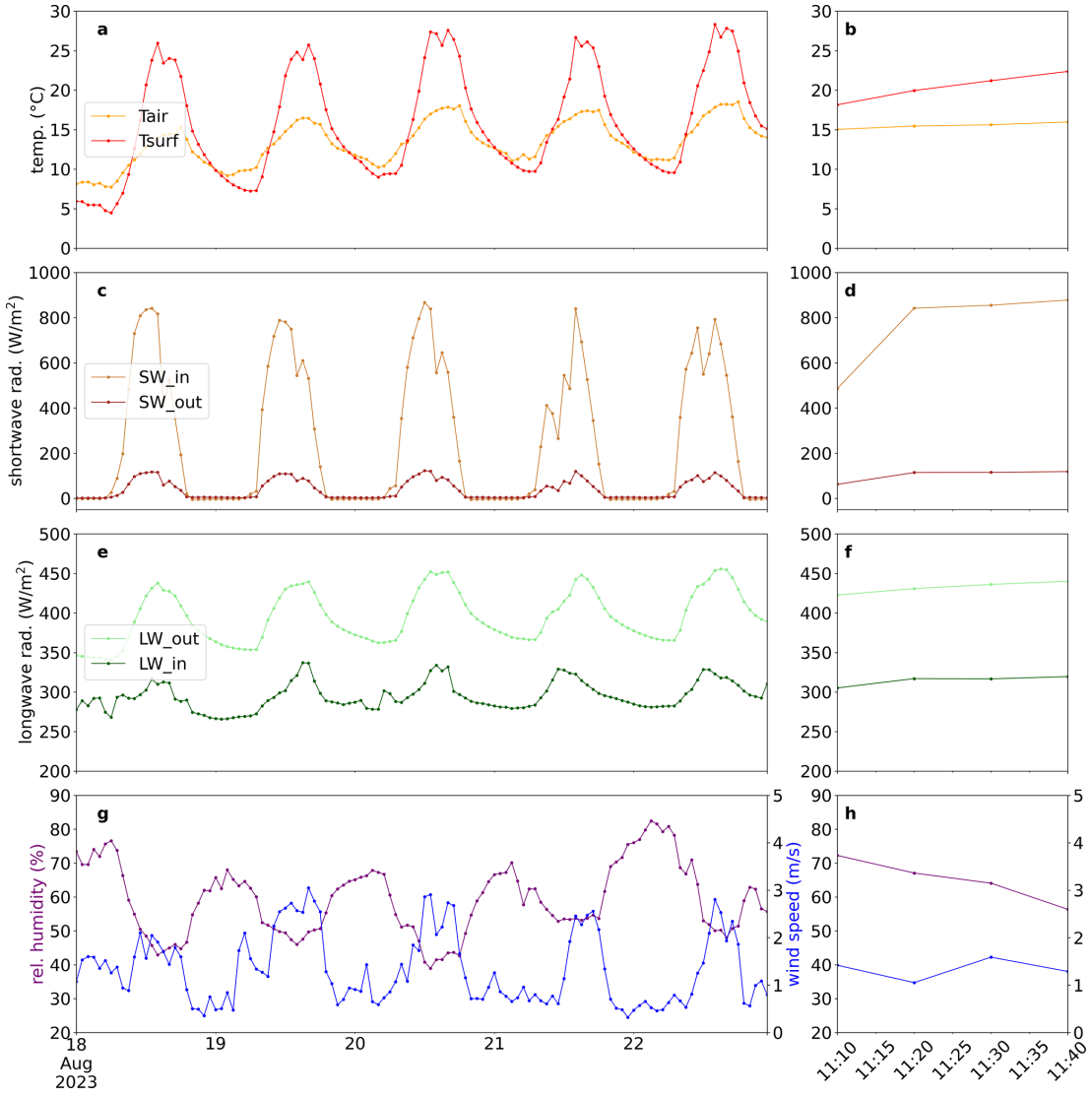

Figure A2. Meteorological conditions at the AWS on the Murtèl rock glacier on the survey day plus 4 d prior (left) and during the survey (right, time shown is GPS time) in 2023 for air and surface temperature **(a, b)**, incoming and outgoing shortwave radiation **(c, d)**, incoming and outgoing longwave radiation **(e, f)**, and relative humidity and wind speed **(g, h)**.

A2 Sensitivity analysis – orthomosaic statistics

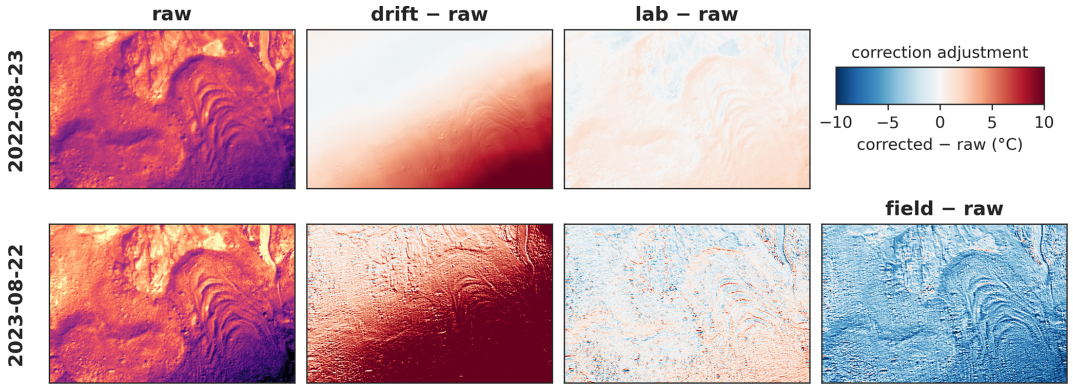

Figure A3. Correction adjustment per approach illustrated as difference from the raw orthomosaic from both survey years (top: 2022, bottom: 2023) and varying correction schemes (drift, lab and field) shown in Fig. 8.

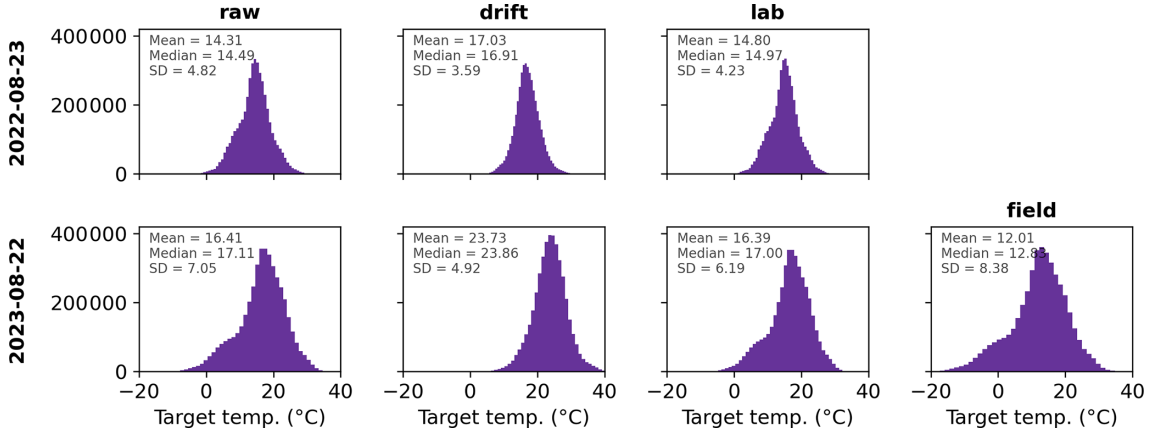

Figure A4. Histograms of pixel temperatures of the thermal orthomosaics from both survey years (top: 2022, bottom: 2023) and varying correction schemes (drift, lab and field) shown in Fig. 8.

Table A1. Statistics of each individual TIR orthomosaic and the impact of the individual correction schemes compared to the reference orthomosaic (raw).

	TIR OM	Mean [°C]	Med [°C]	SD [°C]	Var [°C^2]	Min [°C]	Max [°C]	Rng [°C]	Diff [%]	Var Diff [°C^2]
23 August 2022	raw	14.31	14.49	4.82	23.21	−4.65	32.90	37.54	–	–
	drift	17.03	16.91	3.59	12.89	4.56	33.80	29.24	19.02	10.11
	lab	14.80	14.97	4.23	17.86	−1.63	31.46	33.09	3.48	0.37
22 August 2023	raw	16.41	17.11	7.05	49.67	−19.61	39.35	58.95	–	–
	drift	23.73	23.86	4.92	24.21	−3.88	46.21	50.08	44.63	26.64
	lab	16.39	17.00	6.19	38.35	−15.10	36.36	51.46	−0.11	4.42
	field	12.01	12.83	8.38	70.23	−31.40	39.00	70.40	−26.80	6.66

A3 Variability at validation locations

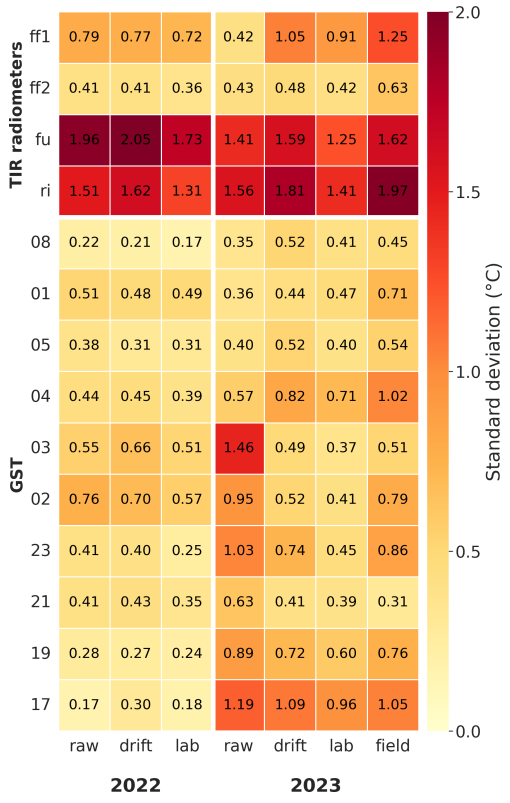

Figure A5. Heatmap of the standard deviation at the in situ locations for 2022 (left three columns) and 2023 (right four columns). Higher values indicate greater local thermal heterogeneity and potentially greater spatial representativeness uncertainty when comparing the UAV TIR OM temperatures with an individual in situ measurement; they do not directly quantify validation error or correction performance.

A4 GST diurnal variability on the survey days

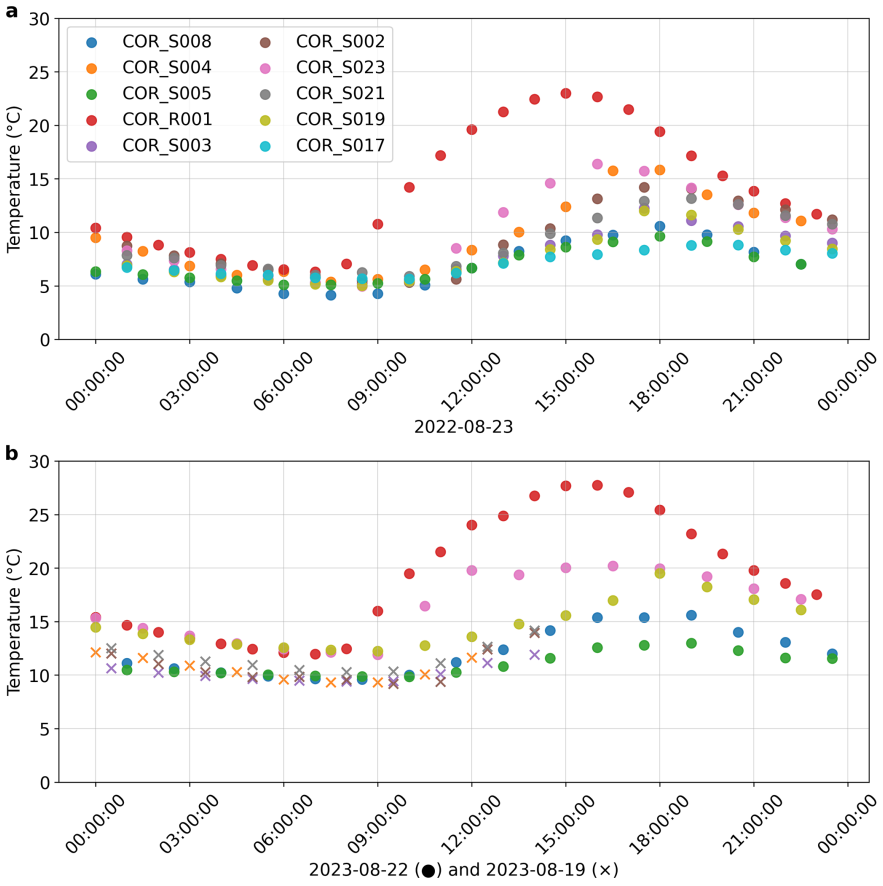

Figure A6. **(a)** GST diurnal cycle on 23 August 2022 for all loggers, and **(b)** on 22 August 2023 for COR_S008, S005, S019, S023, R001 (dots), and on 19 August 2023 for COR_S002, S003, S004, S021 (crosses).

A5 Topographic impact assessment

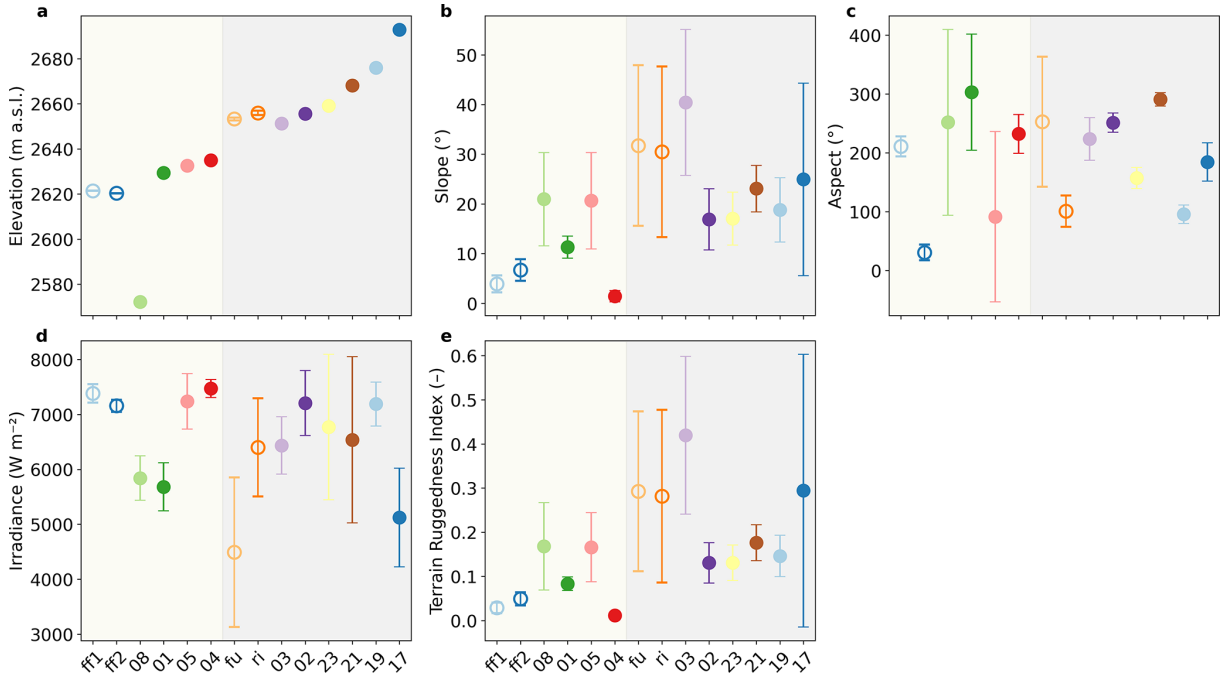

Figure A7. Topographic characteristics elevation **(a)**, slope **(b)**, aspect **(c)**, irradiance **(d)** and Terrain Ruggedness Index (TRII) **(e)** at each in situ location. GST locations are depicted as dots, TIR radiometer locations as circles. Errorbars indicate the standard deviation of all values extracted within the footprint of each location. The beige shaded area comprises instruments located in the forefield or on the relict rock glacier, while the grey shaded area comprises all instruments located on the active rock glacier.

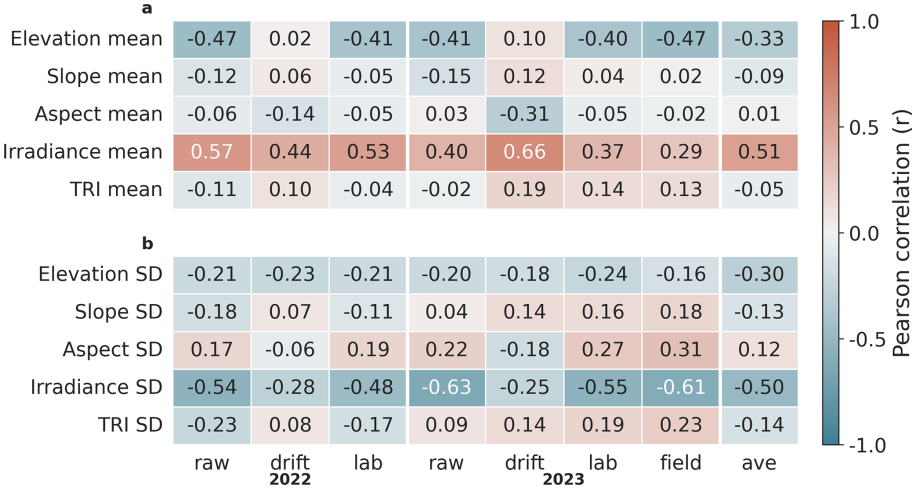

Figure A8. Pearson correlation coefficients between in situ and UAV TIR absolute temperature differences and topographic factors. **(a)** Mean values of elevation, slope, aspect, irradiance, and Terrain Ruggedness Index (TRI). **(b)** Standard deviations of the same factors, representing local heterogeneity. Positive and negative correlations are displayed in red and blue, respectively.

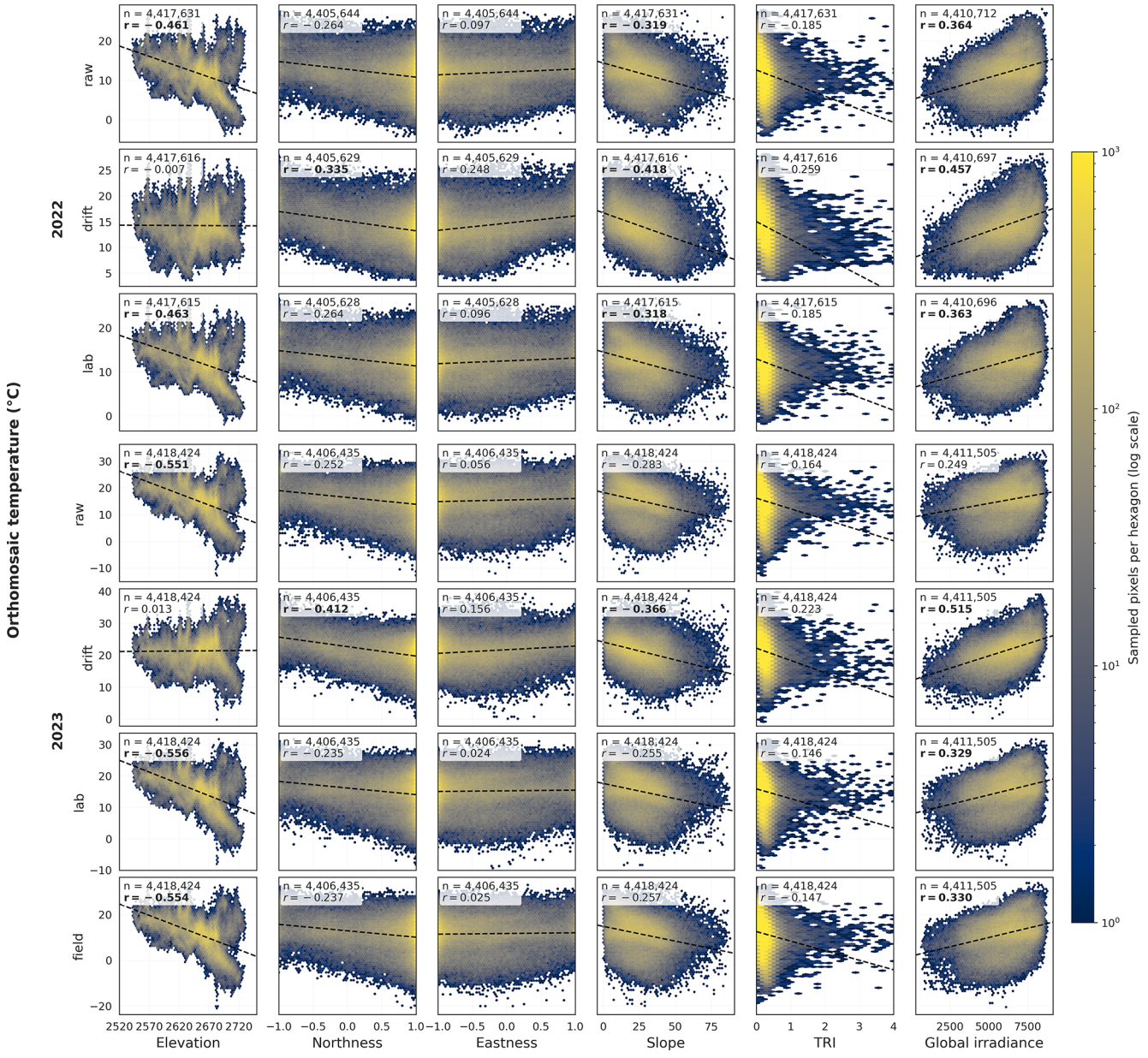

Figure A9. Surface temperature–topography relationship matrix for the raw and corrected TIR OMs in 2022 (top three rows) and 2023 (bottom four rows).

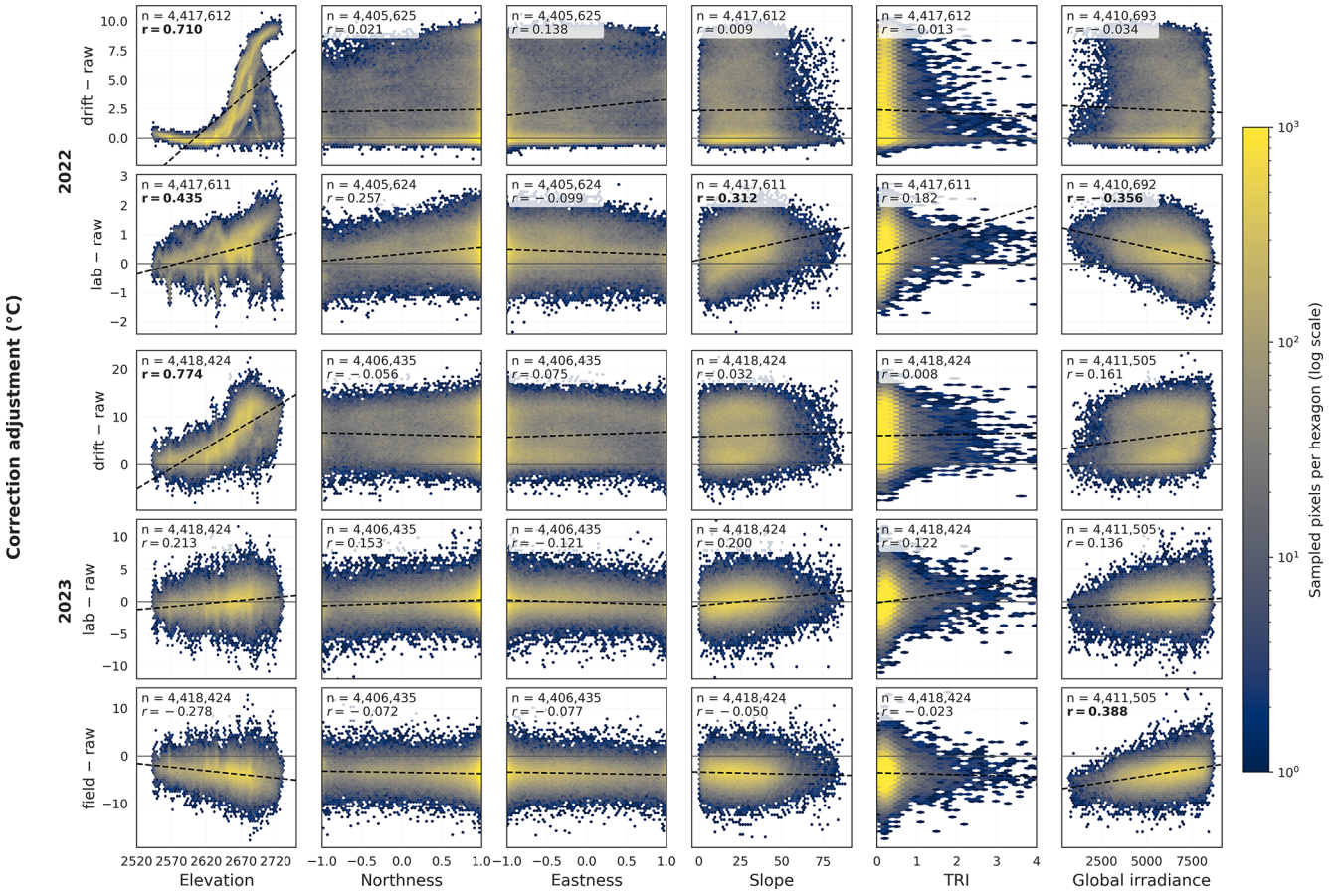

Figure A10. Correction adjustment (correction TIR OM minus raw TIR OM)–topography relationship matrix in 2022 (top two rows) and 2023 (bottom three rows).

Data availability. The PERMOS data can be obtained from the PERMOS webpage (https://doi.org/10.13093/permos-2025-01, PERMOS, 2025a, b). All UAV data used and produced through this study are available upon request.

Author contributions. KN: Writing – original draft, Writing – review & editing, Visualization, Validation, Methodology, Investigation, Formal analysis, Data acquisition & curation, Conceptualization. JSA: Writing – review & editing, Visualization, Validation, Methodology, Investigation, Formal analysis, Data acquisition & curation, Conceptualization. GB: Writing – review & editing, Data acquisition. IGR: Writing – review & editing, Validation, Data acquisition & curation. JG: Writing – review & editing, Validation, Methodology, Data acquisition & curation. NR: Writing – review & editing, Visualization, Validation, Methodology, Investigation, Formal analysis, Data acquisition & curation. Apart from the first author, the authors are listed in alphabetical order.

Competing interests. The contact author has declared that none of the authors has any competing interests.

Disclaimer. Publisher's note: Copernicus Publications remains neutral with regard to jurisdictional claims made in the text, published maps, institutional affiliations, or any other geographical representation in this paper. The authors bear the ultimate responsibility for providing appropriate place names. Views expressed in the text are those of the authors and do not necessarily reflect the views of the publisher.

Authors' note. The authors declare that all UAV operations conducted for data acquisition were performed in accordance with applicable regulations and any required permits or authorisations in force at the time and location of each flight.

Acknowledgements. KN, JSA and NR are supported by the ESA PRODEX Trishna T-SEC project (PEA C4000133711). GB is supported by the SNSF Ambizione project grant no. 216385. We like to thank an anonymous reviewer and Luc Girod for their constructive feedback, which has improved the manuscript.

Financial support. This research has been supported by the European Space Agency (grant no. PEA C4000133711) and the Swiss National Science Foundation (grant no. 216385).

Review statement. This paper was edited by Andreas Kääb and reviewed by Luc Girod and one anonymous referee.

References

Adams, J. S., Damm, A., Werfeli, M., Gröbner, J., and Naegeli, K.: Across-scale thermal infrared anisotropy in forests: Insights from a multi-angular laboratory-based approach, Remote Sens. Environ., 326, 114766, https://doi.org/10.1016/J.RSE.2025.114766, 2025.

Aragon, B., Johansen, K., Parkes, S., Malbeteau, Y., Al-mashharawi, S., Al-amoudi, T., Andrade, C. F., Turner, D., Lucieer, A., and McCabe, M. F.: A Calibration Procedure for Field and UAV-Based Uncooled Thermal Infrared Instruments, Sensors 2020, 20, 3316, https://doi.org/10.3390/S20113316, 2020.

Arioli, S., Picard, G., Arnaud, L., Gascoin, S., Alonso-González, E., Poizat, M., and Irvine, M.: Time series of alpine snow surface radiative-temperature maps from high-precision thermal-infrared imaging, Earth Syst. Sci. Data, 16, 3913–3934, https://doi.org/10.5194/essd-16-3913-2024, 2024.

Aubrecht, D. M., Helliker, B. R., Goulden, M. L., Roberts, D. A., Still, C. J., and Richardson, A. D.: Continuous, long-term, high-frequency thermal imaging of vegetation: Uncertainties and recommended best practices, Agr. Forest Meteorol., 228–229, 315–326, https://doi.org/10.1016/j.agrformet.2016.07.017, 2016.

Aubry-Wake, C., Lamontagne-Hallé, P., Baraër, M., McKenzie, J. M., and Pomeroy, J. W.: Using ground-based thermal imagery to estimate debris thickness over glacial ice: fieldwork considerations to improve the effectiveness, J. Glaciol., 1–17, https://doi.org/10.1017/jog.2022.67, 2022.

Bhardwaj, A., Sam, L., Akanksha, Martín-Torres, F. J., and Kumar, R.: UAVs as remote sensing platform in glaciology: Present applications and future prospects, Remote Sens. Environ., 175, 196–204, https://doi.org/10.1016/J.RSE.2015.12.029, 2016.

Bisset, R. R., Nienow, P. W., Goldberg, D. N., Wigmore, O., Loayza-Muro, R. A., Wadham, J. L., Macdonald, M. L., and Bingham, R. G.: Using thermal UAV imagery to model distributed debris thicknesses and sub-debris melt rates on debris-covered glaciers, J. Glaciol., 69, 981–996, https://doi.org/10.1017/JOG.2022.116, 2023.

Brenning, A., Peña, M. A., Long, S., and Soliman, A.: Thermal remote sensing of ice-debris landforms using ASTER: an example from the Chilean Andes, The Cryosphere, 6, 367–382, https://doi.org/10.5194/tc-6-367-2012, 2012.

Casas-Mulet, R., Pander, J., Ryu, D., Stewardson, M. J., and Geist, J.: Unmanned Aerial Vehicle (UAV)-Based Thermal Infra-Red (TIR) and Optical Imagery Reveals Multi-Spatial Scale Controls of Cold-Water Areas Over a Groundwater-Dominated Riverscape, Front. Environ. Sci., 8, 534986, https://doi.org/10.3389/FENVS.2020.00064, 2020.

Cawse-Nicholson, K., Townsend, P. A., Schimel, D., Assiri, A. M., Blake, P. L., Buongiorno, M. F., Campbell, P., Carmon, N., Casey, K. A., Correa-Pabón, R. E., Dahlin, K. M., Dashti, H., Dennison, P. E., Dierssen, H., Erickson, A., Fisher, J. B., Frouin, R., Gatebe, C. K., Gholizadeh, H., Gierach, M., Glenn, N. F., Goodman, J. A., Griffith, D. M., Guild, L., Hakkenberg, C. R., Hochberg, E. J., Holmes, T. R., Hu, C., Hulley, G., Huemmrich, K. F., Kudela, R. M., Kokaly, R. F., Lee, C. M., Martin, R., Miller, C. E., Moses, W. J., Muller-Karger, F. E., Ortiz, J. D., Otis, D. B., Pahlevan, N., Painter, T. H., Pavlick, R., Poulter, B., Qi, Y., Realmuto, V. J., Roberts, D., Schaepman, M. E., Schneider, F. D., Schwandner, F. M., Serbin, S. P., Shiklomanov, A. N., Stavros, E. N., Thompson, D. R., Torres-Perez, J. L., Turpie, K. R., Tzortziou, M., Ustin, S., Yu, Q., Yusup, Y., and Zhang, Q.: NASA's surface biology and geology designated observable: A perspective on surface imaging algorithms, Remote Sens. Environ., 257, 112349, https://doi.org/10.1016/J.RSE.2021.112349, 2021.

Colombo, R., Pennati, G., Pozzi, G., Garzonio, R., Di Mauro, B., Giardino, C., Cogliati, S., Rossini, M., Maltese, A., Pogliotti, P., and Cremonese, E.: Mapping snow density through thermal inertia observations, Remote Sens. Environ., 284, 113323, https://doi.org/10.1016/J.RSE.2022.113323, 2023.

Colomina, I. and Molina, P.: Unmanned aerial systems for photogrammetry and remote sensing: A review, ISPRS J. Photogramm., 92, 79–97, https://doi.org/10.1016/J.ISPRSJPRS.2014.02.013, 2014.

Crago, R. D. and Qualls, R. J.: Use of land surface temperature to estimate surface energy fluxes: Contributions of Wilfried Brutsaert and collaborators, Water Resour. Res., 50, 3396–3408, https://doi.org/10.1002/2013WR015223, 2014.

Dugdale, S. J., Kelleher, C. A., Malcolm, I. A., Caldwell, S., and Hannah, D. M.: Assessing the potential of drone-based thermal infrared imagery for quantifying river temperature heterogeneity, Hydrol. Process., 33, 1152–1163, https://doi.org/10.1002/HYP.13395, 2019.

Elfarkh, J., Johansen, K., Angulo, V., Camargo, O. L., and McCabe, M. F.: Quantifying Within-Flight Variation in Land Surface Temperature from a UAV-Based Thermal Infrared Camera, Drones, 7, 617, https://doi.org/10.3390/DRONES7100617, 2023.

Gärtner-Roer, I. and Hoelzle, M.: Rockglaciers of the Engadine, World Geomorphological Landscapes, 235–248, https://doi.org/10.1007/978-3-030-43203-4_16, 2021.

Gök, D. T., Scherler, D., and Anderson, L. S.: High-resolution debris-cover mapping using UAV-derived thermal imagery: limits and opportunities, The Cryosphere, 17, 1165–1184, https://doi.org/10.5194/tc-17-1165-2023, 2023.

Gröbner, J.: Operation and investigation of a tilted bottom cavity for pyrgeometer characterizations, Appl. Optics, 47, 4441–4447, https://doi.org/10.1364/AO.47.004441, 2008.

Groos, A. R., Aeschbacher, R., Fischer, M., Kohler, N., Mayer, C., and Senn-Rist, A.: Accuracy of UAV Photogrammetry in Glacial and Periglacial Alpine Terrain: A Comparison With Airborne and Terrestrial Datasets, Front. Remote Sens., 3, 871994, https://doi.org/10.3389/FRSEN.2022.871994, 2022.

Hoelzle, M., Hauck, C., Mathys, T., Noetzli, J., Pellet, C., and Scherler, M.: Long-term energy balance measurements at three different mountain permafrost sites in the Swiss Alps, Earth Syst. Sci. Data, 14, 1531–1547, https://doi.org/10.5194/essd-14-1531-2022, 2022.

Hook, S. J., Johnson, W. R., and Abrams, M. J.: NASA's Hyperspectral Thermal Emission Spectrometer (HyTES), Re-

mote Sensing and Digital Image Processing, 17, 93–115, https://doi.org/10.1007/978-94-007-6639-6_5, 2013.

Huo, D., Bishop, M. P., and Bush, A. B.: Understanding Complex Debris-Covered Glaciers: Concepts, Issues, and Research Directions, Front. Earth Sci., 9, 652279, https://doi.org/10.3389/FEART.2021.652279, 2021.

Kelly, J., Kljun, N., Olsson, P. O., Mihai, L., Liljeblad, B., Weslien, P., Klemedtsson, L., and Eklundh, L.: Challenges and best practices for deriving temperature data from an uncalibrated UAV thermal infrared camera, Remote Sens., 11, https://doi.org/10.3390/rs11050567, 2019.

Koetz, B., Bastiaanssen, W., Berger, M., Defourney, P., Bello, U. D., Drusch, M., Drinkwater, M., Duca, R., Fernandez, V., Ghent, D., Guzinski, R., Hoogeveen, J., Hook, S., Lagouarde, J. P., Lemoine, G., Manolis, I., Martimort, P., Masek, J., Massart, M., Notarnicola, C., Sobrino, J., and Udelhoven, T.: High spatio-temporal resolution land surface temperature mission - A copernicus candidate mission in support of agricultural monitoring, International Geoscience and Remote Sensing Symposium (IGARSS), July 2018, 8160–8162, https://doi.org/10.1109/IGARSS.2018.8517433, 2018.

Kraaijenbrink, P. D., Shea, J. M., Pellicciotti, F., Jong, S. M., and Immerzeel, W. W.: Object-based analysis of unmanned aerial vehicle imagery to map and characterise surface features on a debris-covered glacier, Remote Sens. Environ., 186, 581–595, https://doi.org/10.1016/J.RSE.2016.09.013, 2016.

Kraaijenbrink, P. D., Shea, J. M., Litt, M., Steiner, J. F., Treichler, D., Koch, I., and Immerzeel, W. W.: Mapping surface temperatures on a debris-covered glacier with an unmanned aerial vehicle, Front. Earth Sci., 6, https://doi.org/10.3389/feart.2018.00064, 2018.

Lillesand, T., Kiefer, R. W., and Chipman, J. W.: Remote Sensing and Image Interpretation, John Wiley & Sons Ltd, 7th edn., ISBN 978-1-118-34328-9, 2015.

Lin, D., Maas, H. G., Westfeld, P., Budzier, H., and Gerlach, G.: An advanced radiometric calibration approach for uncooled thermal cameras, Photogramm. Rec., 33, 30–48, https://doi.org/10.1111/PHOR.12216, 2018.

Liu, Y., Hiyama, T., and Yamaguchi, Y.: Scaling of land surface temperature using satellite data: A case examination on ASTER and MODIS products over a heterogeneous terrain area, Remote Sens. Environ., 105, 115–128, https://doi.org/10.1016/J.RSE.2006.06.012, 2006.

Maes, W. H. and Steppe, K.: Estimating evapotranspiration and drought stress with ground-based thermal remote sensing in agriculture: a review, J. Exp. Bot., 63, 4671–4712, https://doi.org/10.1093/jxb/ers165, 2012.

Maes, W. H., Huete, A. R., and Steppe, K.: Optimizing the processing of UAV-based thermal imagery, Remote Sens., 9, https://doi.org/10.3390/rs9050476, 2017.

Malbéteau, Y., Johansen, K., Aragon, B., Al-Mashhawari, S. K., and McCabe, M. F.: Overcoming the Challenges of Thermal Infrared Orthomosaics Using a Swath-Based Approach to Correct for Dynamic Temperature and Wind Effects, Remote Sens., 13, 3255, https://doi.org/10.3390/RS13163255, 2021.

Mesas-Carrascosa, F. J., Pérez-Porras, F., de Larriva, J. E. M., Frau, C. M., Agüera-Vega, F., Carvajal-Ramírez, F., Martínez-Carricondo, P., and García-Ferrer, A.: Drift Correction of Lightweight Microbolometer Thermal Sensors On-Board Unmanned Aerial Vehicles, Remote Sens., 10, 615, https://doi.org/10.3390/RS10040615, 2018.

Messmer, J. and Groos, A. R.: A low-cost and open-source approach for supraglacial debris thickness mapping using UAV-based infrared thermography, The Cryosphere, 18, 719–746, https://doi.org/10.5194/tc-18-719-2024, 2024.

Mineo, S. and Pappalardo, G.: Rock Emissivity Measurement for Infrared Thermography Engineering Geological Applications, Appl. Sci., 11, 3773, https://doi.org/10.3390/APP11093773, 2021.

O'Sullivan, A. M. and Kurylyk, B. L.: Limiting External Absorptivity of UAV-Based Uncooled Thermal Infrared Sensors Increases Water Temperature Measurement Accuracy, Remote Sens., 14, https://doi.org/10.3390/rs14246356, 2022.

Pepin, N., Apple, M., Knowles, J., Terzago, S., Arnone, E., Hänchen, L., Napoli, A., Potter, E., Steiner, J., Williamson, S. N., Ahrens, B., Dhar, T., Dimri, A. P., Palazzi, E., Rameshan, A., Salzmann, N., Shahgedanova, M., de Deus Vidal, J., and Zardi, D.: Elevation-dependent climate change in mountain environments, Nat. Rev. Earth Environ., 6, 772–788, https://doi.org/10.1038/s43017-025-00740-4, 2025.

Pepin, N. C., Arnone, E., Gobiet, A., Haslinger, K., Kotlarski, S., Notarnicola, C., Palazzi, E., Seibert, P., Serafin, S., Schöner, W., Terzago, S., Thornton, J. M., Vuille, M., and Adler, C.: Climate Changes and Their Elevational Patterns in the Mountains of the World, Rev. Geophys., 60, e2020RG000730, https://doi.org/10.1029/2020RG000730, 2022.

PERMOS: PERMOS Database, Swiss Permafrost Monitoring Network, Davos and Fribourg, Switzerland [data set], https://doi.org/10.13093/permos-2025-01, 2025a.

PERMOS: Swiss Permafrost Bulletin 2024, edited by: Noetzli, J. and Pellet, C., No. 6, 29 pp., Swiss Permafrost Monitoring Network, Davos and Fribourg, Switzerland, https://doi.org/10.13093/permos-bull-2025, 2025b.

Pignatti, S., Lapenna, V., Palombo, A., Pascucci, S., Pergola, N., and Cuomo, V.: An advanced tool of the CNR IMAA EO facilities: Overview of the TASI-600 hyperspectral thermal spectrometer, Workshop on Hyperspectral Image and Signal Processing, Evolution in Remote Sensing, https://doi.org/10.1109/WHISPERS.2011.6080890, 2011.

Rietze, N., Assmann, J. J., Plekhanova, E., Naegeli, K., Damm, A., Maximov, T. C., Karsanaev, S. V., Hensgens, G., and Schaepman-Strub, G.: Summer drought weakens land surface cooling of tundra vegetation, Environ. Res. Lett., 19, 044043, https://doi.org/10.1088/1748-9326/AD345E, 2024.

Riley, S. J., DeGloria, S. D., and Elliot, R.: A terrain ruggedness index that quantifies topographic heterogeneity, Intermountain Journal of Science, 5, 23–27, 1999.

Roujean, J. L., Bhattacharya, B., Gamet, P., Pandya, M. R., Boulet, G., Olioso, A., Singh, S. K., Shukla, M. V., Mishra, M., Babu, S., Raju, P. V., Murthy, C. S., Briottet, X., Rodler, A., Autret, E., Dadou, I., Adlakha, D., Sarkar, M., Picard, G., Kouraev, A., Ferrari, C., Irvine, M., Delogu, E., Vidal, T., Hagolle, O., Maisongrande, P., Sekhar, M., and Mallick, K.: TRISHNA: An Indo-French Space Mission to Study the Thermography of the Earth at Fine Spatio-Temporal Resolution, 2021 IEEE India Geoscience and Remote Sensing Symposium, InGARSS 2021 – Proceedings, 49–52, https://doi.org/10.1109/INGARSS51564.2021.9791925, 2021.

Rubio, E., Caselles, V., and Badenas, C.: Emissivity measurements of several soils and vegetation types in the 8–14 µm Wave band: Analysis of two field methods, Remote Sens. Environ., 59, 490–521, https://doi.org/10.1016/S0034-4257(96)00123-X, 1997.

Saibene, G., Gärtner-Roer, I., Beutel, J., and Vieli, A.: Multi-annual and seasonal patterns of Murtèl rock glacier borehole deformation, environmental controls and implications for kinematic monitoring, The Cryosphere, 20, 3511–3532, https://doi.org/10.5194/tc-20-3511-2026, 2026.

Tattersall, G.: gtatters/Thermimage: Thermimage v4.1.3, Zenodo [code], https://doi.org/10.5281/zenodo.5525416, 2021.

Tricht, L. V., Zekollari, H., Huss, M., Rounce, D. R., Schuster, L., Aguayo, R., Schmitt, P., Maussion, F., Tober, B., and Farinotti, D.: Peak glacier extinction in the mid-twenty-first century, Nat. Clim. Change, 16, 143–147, https://doi.org/10.1038/s41558-025-02513-9, 2025.

Wan, Q., Smigaj, M., Brede, B., and Kooistra, L.: Optimizing UAV-based uncooled thermal cameras in field conditions for precision agriculture, Int. J. Appl. Earth Obs., 134, 104184, https://doi.org/10.1016/J.JAG.2024.104184, 2024.

Wang, Z., Zhou, J., Ma, J., Wang, Y., Liu, S., Ding, L., Tang, W., Pakezhamu, N., and Meng, L.: Removing temperature drift and temporal variation in thermal infrared images of a UAV uncooled thermal infrared imager, ISPRS J. Photogramm., 203, 392–411, https://doi.org/10.1016/J.ISPRSJPRS.2023.08.011, 2023.

Wigmore, O. and Molotch, N. P.: Weekly high-resolution multi-spectral and thermal uncrewed-aerial-system mapping of an alpine catchment during summer snowmelt, Niwot Ridge, Colorado, Earth Syst. Sci. Data, 15, 1733–1747, https://doi.org/10.5194/essd-15-1733-2023, 2023.